Topological Hall effect in strongly correlated layered magnets: The effect of the spin of the magnetic atoms and of the polar and azimuthal angles subtended by the spin texture

Kaushal Kumar Kesharpu [*]

Bogoliubov Laboratory of Theoretical Physics, Joint Institute for Nuclear Research, Dubna 141980, Russia

The topological properties are investigated for strongly correlated materials having honeycomb lattice structures and spin texture $\vec{S} = S[\sin(\vec{q}_1\vec{r})\cos(\vec{q}_2\vec{r}), \sin(\vec{q}_1\vec{r})\sin(\vec{q}_2\vec{r}), \cos(\vec{q}_1\vec{r})]$; here, $\vec{q}_1$ (polar) and $\vec{q}_2$ (azimuthal) are the spin modulating vectors and S is the spin (total angular momentum) of the magnetic atoms. The results can be applied to materials showing the Kondo lattice behavior within the strong Kondo coupling regime. The explicit dependence of the Chern number on $\vec{q}_1$, $\vec{q}_2$ for $S = 1, 2, 3$ and $S = 1/2, 3/2, 5/2$ (in limiting cases) is derived. We find that for $S = 1, 2, 3$, the Chern number depends strongly on $\vec{q}_2$ and S; and for $S = 1/2, 3/2, 5/2$, the same dependence is expected. The main physical effect of our result is the change in the direction of the topological Hall resistivity ($+\rho_{xy}^{\text{THE}} \rightarrow -\rho_{xy}^{\text{THE}}$ or vice versa, THE stands for the topological Hall effect) when $S > 2$ as the wave vectors are modulated. We propose heterostructures involving the iron based van der Waals magnet $Fe_{N=3,4,5}GeTe_2$, because in this material both the investigated spin texture and Kondo lattice behavior were observed. Our method can also be applied to materials with higher spin $S > 3$ to investigate topological properties.

I. INTRODUCTION

Motion of electrons on an adiabatically changing chiral spin texture in the strong coupling regime gives rise to the topological Hall effect (THE) [1]. For the strong coupling case, the spin of the electrons follows the local direction of the magnetization. If the magnetization varies in a closed loop, then the electrons acquire a geometric phase in the parameter space, which in turn gives rise to the THE [2,3]. A large number of spin textures—e.g., skyrmions, conical, hedgehog, magnetic bubble, to name a few (or a complete list see Table 1 of Ref. [3])—generating THE were observed experimentally in 2D layered magnetic materials [3]. Microscopically, the Dzyloshinskii-Moriya interaction (DMI) [4,5], the dipolar interaction [6], frustrated chirality [7,8], out-of-plane anisotropy [9,10], and Fermi surface curvatures [11] are responsible for generating noncollinear spin texture, in turn THE. Due to the involvement of these different microscopic effects, understanding the competition between them [12–15] and ways to manipulate them is important from the point of view of the fundamental physics as well as applied spintronics [16]. Recently, Van der Waals (VdW) magnets have emerged as one of the promising class of materials for investigation of these effects [17], due to the possibility of changing their properties through intrinsic means (chemical doping [18], stacking order and twist of the monolayers [17,19–22]), and extrinsic means (electric and magnetic field, strain, pressure [23]). The VdW magnets are primarily divided into five different family of compounds [18,24]: (i) transition metal halides, (ii) transition metal phosphorous trichalcogenides, (iii) transition metal di-chalcogenides, (iv) ternary iron based tellurides,

and (v) transition metal oxyhalides. In these compounds itinerant ferromagnetism, the Kondo lattice behavior and Mott insulating phase are observed due to the strong electronic correlation [24–30]. Keeping this in mind, an investigation of the electronic properties of these 2D materials with localized spin moments a low-energy effective theory using $su(2)$ path integral method was proposed recently [31]. It was shown that the THE for a material with a honeycomb bipartite lattice and a strongly coupled electron spin to the background high-spin S conical spin texture depends only on the (i) atomic spin S (ii) and the spin modulation vector of the spin texture. On a side note, by S we mean multiplet of localized angular momentum $\vec{j} = \vec{l} + \vec{s}$ due to spin-orbit coupling. For example, a Ce^{3+} ions contains a single unpaired $4f$ electrons in the state $4f^1$ with $l = 3$ and $s = 1/2$. The spin-orbit coupling gives rise to the low-lying multiplet with $j = 3 - 1/2 = 5/2$. In our case, j and S are same. In the investigated conical spin texture, only the azimuthal angle of the spin projection (on xy plane) changed through neighboring sites. Hence naturally the question arises: how the topological properties of the materials changes if both the azimuthal angle as well as the polar angle of the spin texture change? To answer this question in this work, we analyzed the spin texture:

$$\vec{S}_i \equiv \begin{bmatrix} S_x \\ S_y \\ S_z \end{bmatrix} = S \begin{bmatrix} \sin \vec{q}_1\vec{r}_i & \cos \vec{q}_2\vec{r}_i \\ \sin \vec{q}_1\vec{r}_i & \sin \vec{q}_2\vec{r}_i \\ & \cos \vec{q}_1\vec{r}_i \end{bmatrix}. \quad (1)$$

Here, S_x, S_y, and S_z are the x, y, and z components of the localized spin momentum $\vec{S}_i$. $\vec{q}_1 = (q_{1x}, q_{1y})$ and $\vec{q}_2 = (q_{2x}, q_{2y})$ are the two spin modulating wave vectors on a 2D plane. $\vec{r}_i = (x, y)$ is the position vector on the 2D plane. The spin texture on a different lattice structure is shown in Fig. 1.

The experimentally analogous spin texture was observed in VdW ferromagnet Fe_3GeTe_2 (F3GT). It is a conductor

*kesharpu@theor.jinr.ru

(a) Square

(b) Triangular
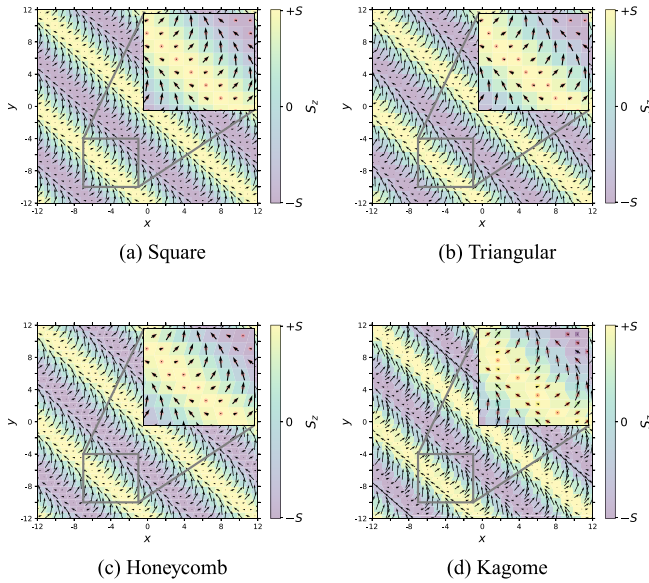
(c) Honeycomb

(d) Kagome

FIG. 1. Spin texture generated from Eq. (1) for $\vec{q}_1 = \vec{q}_2 = (\pi/6, \pi/6)$ on (a) square, (b) triangular, (c) honeycomb, and (d) Kagome lattices. The direction of the arrow represents the angle extended by S_x and S_y on xy plane, defined as $\arctan(S_y/S_x)$. The color represents the values of the S_z.

with itinerant ferromagnetism [34] and Kondo lattice behavior [35]. In F3GT using scanning electron microscopy with polarization analysis, a modulated spin spiral on the xz plane (Neel order), as well as on the xy plane, was observed [32]. The same spin texture was also observed through Lorentz transmission electron microscopy (LTEM) and micromagnetic simulations [36–38]. In Fig. 2(a) using Eq. (1) with $\vec{q}_1 = (\pi/8, \pi/8)$ and $\vec{q}_2 = (\pi/4, \pi/4)$, we plot a qualitatively same spin texture as was experimentally observed (see Fig. 1 of Ref. [32]). We say qualitatively, as one can see the pronounced peak and dip of the magnetization for $S_z + S_x$ in comparison to $S_z + S_y$, as was observed in experiment. In another sister compound $Cr_2Ge_2Te_6$ (CGT) through LTEM, the analogous spin texture was detected [33]. In Fig. 2(b) using Eq. (1) for $\vec{q}_1 = (\pi/2, 0)$ and $\vec{q}_2 = (\pi/3, 0)$, we reproduce the experimentally observed spin texture (see Fig. 2(c) of Ref. [33]). Physically this spin texture can be thought of as Neel spin order sandwiched in between two Bloch domain walls. Besides, such a magnetic texture was also observed in heterostructures of the multiple ferromagnetic monolayers. In these materials, the combined effect of the perpendicular magnetic anisotropy (PMA)—due to the dipole interaction between the layers—and the interfacial DMI gives rise to the spin texture [39]. In $[Co/Ni]_n/Ir/Pt(111)$ heterostructure, depending on the thickness of the magnetic multilayer stack $[Co/Ni]_n$ and the Ir layer, either Bloch-type or Neel-type domain walls were observed, however, for some specific thickness of both these layers one can find both Bloch and Neel domain walls [40]. It is in this region one can find the spin texture represented by Eq. (1). The same is true for Co/Pd [41] and Fe/Ni/Cu(001) [42] multilayers.

In this work, we solve the Hamiltonian of the 2D magnetic materials in the strong electron correlation limit with spin
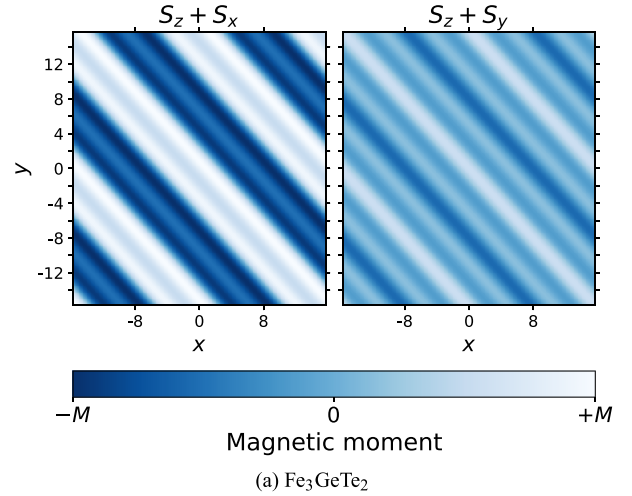
(a) Fe_3GeTe_2
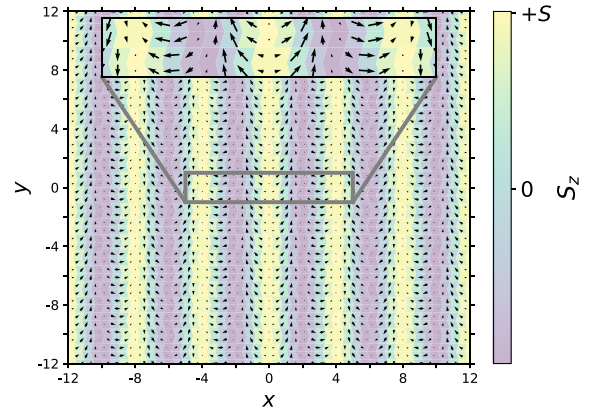
(b) $Cr_2Ge_2Te_6$

FIG. 2. (a) Generation of the qualitative spin texture in Fe_3GeTe_2 experimentally observed in Fig. 1 of Ref. [32] using Eq. (1). On the left-hand side, the summation of magnetization along z and x axes ($S_z + S_x$) is plotted. On the right, the summation of magnetization along z and y axes ($S_z + S_y$) is plotted. We observe more pronounced magnetic texture for $S_z + S_x$ compared to $S_z + S_y$; the same was observed in experiment. (b) Generation of the experimentally observed spin texture in $Cr_2Ge_2Te_6$ in Fig. 2(c) of Ref. [33], using Eq. (1). Here $\vec{q}_1 = (\pi/2, 0)$ and $\vec{q}_2 = (\pi/3, 0)$.

texture given by Eq. (1). It is assumed that the system has a localized high spin S. The high-spin treatment of the problem is necessary, as in most of VdW magnets due to large spin-orbit coupling the angular momentum of the magnetic atom becomes large. Besides, in 2D materials due to reduced coordination number of the surface atoms, the localized electronic bands at surface become narrower compared to the bulk; the narrow band favors the localization, exchange splitting, and higher magnetic moments [43].

The paper is structured as follows: in Sec. II, we investigate the topological properties of the Hamiltonian. In Sec. II A, the Hamiltonian on a honeycomb lattice is given; complete derivation, and the mathematical procedure to solve the Hamiltonian is described in Appendixes A and B, respectively. In Secs. II B and II C, we find the Chern number for integer spins. In Sec. II D, we find Chern number for
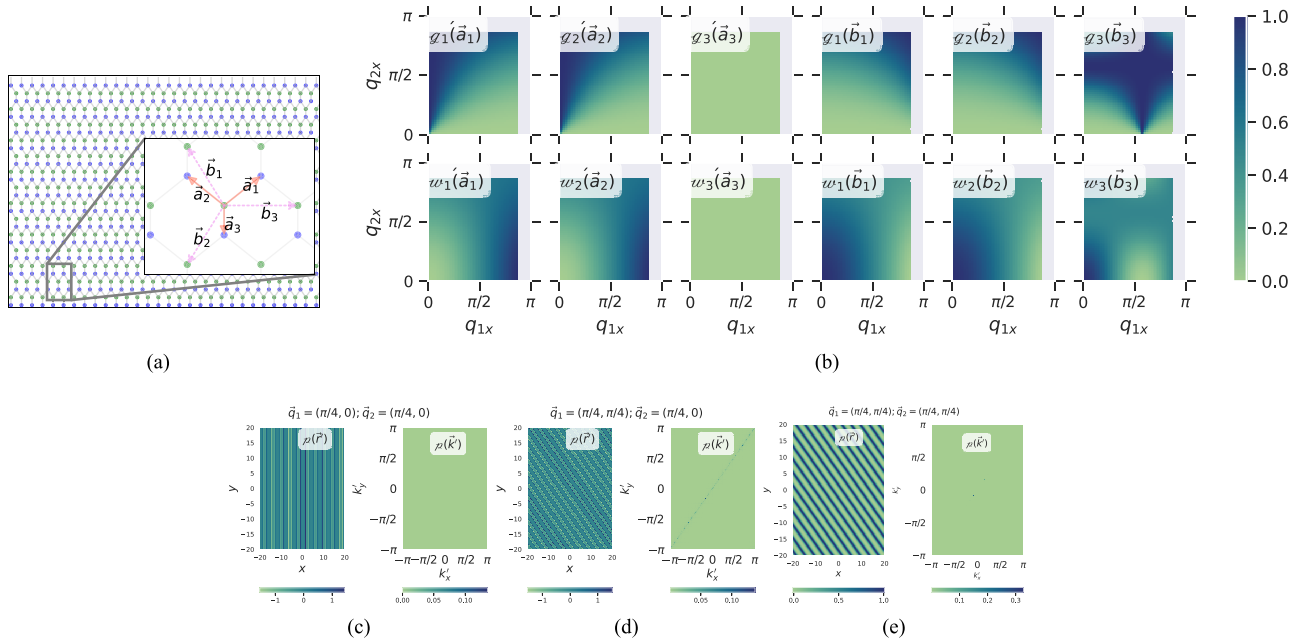
FIG. 3. (a) Schematic of a bipartite honeycomb lattice. $\vec{a}_1$, $\vec{a}_2$, and $\vec{a}_3$ represent the three NN vectors. $\vec{b}_1$, $\vec{b}_2$, and $\vec{b}_3$ represents the three NNN vectors. (b) Plot of the dependence of the g'_n and g_n on the wave vectors $\vec{q}_1 = (2q_{1x}/\sqrt{3}, 0)$ and $\vec{q}_2 = (2q_{2x}/\sqrt{3}, 0)$ for a honeycomb bipartite lattice. It is calculated using Eq. (2). The values of q_{1x} and q_{2x} lies in the range $(0, \sqrt{3}\pi/2)$. [(c)–(e)] Plot of the real space function $\wp(\vec{r}_i)$ and its Fourier transform $\wp(\vec{k}')$ on a honeycomb lattice. It is calculated using Eq. (3).

half-integer spins in limiting cases. In Sec. III, we discuss different aspects of the results, including possible experimental setups.

II. METHOD AND CALCULATION

We start from the Kondo lattice model (KLM) where the magnetic moments are localized at lattice sites.[1] At large Kondo coupling the KLM is identical to the Hubbard model with large electron correlation [44]. The necessary theory for solving this model using $su(2)$ path integral method was given recently [31]. Basically the idea is to represent the KLM in strong coupling regime (the Hubbard model in strong correlation regime) through the Hubbard X^{pq} operators.[2] As there exist one-to-one mapping of the X^{pq} operators to the $su(2)$

---

[1]KLM is derived from the periodic Anderson model in the strong correlation regime [49,65]. Periodic Anderson model takes into account the hybridization of the localized f electrons.

[2]The Hubbard operators $X_i^{pq} \equiv \langle p \| q \rangle$ describes the transition at site from $|p\rangle$ state to $|q\rangle$ state. Under strong correlation there are three different states possible, i.e., states with up-spin $|\uparrow\rangle$, down-spin $|\downarrow\rangle$, and empty site $|0\rangle$. Hence, for example, $X_i^{\uparrow 0}$ represent the transition from empty state to the up-spin state at ith site. In terms of usual electron creation ($c_{i\sigma}^\dagger$), annihilation ($c_{i\sigma}$), and number ($n_{i\sigma} = c_{i\sigma}^\dagger c_{i\sigma}$) operators, the Hubbard operators are represented as

$$X_i^{0\sigma} = c_{i\sigma}(1 - n_{i\sigma'}), \quad X_i^{\sigma 0} = (1 - n_{i\sigma'})c_{i\sigma}^\dagger,$$

$$X_i^{00} = 1 - \sum_\sigma (1 - n_{i\sigma'})c_{i\sigma}^\dagger c_{i\sigma}(1 - n_{i\sigma'}).$$

Above definition of Hubbard operators shows that the no double occupancy condition is satisfied.

coherent state operators $X_{cs}^{pq} = \langle z, f | X^{pq} | z, f \rangle$ [45–47]—here the f and z are the spinless charged fermionic field (holon) and spinful bosonic fields (spinon) respectively—one can transform the X^{pq} Hamiltonian into the coherent symbol X_{cs}^{pq} Hamiltonian. Finally the path integral approach is used to solve the resulting X_{cs}^{pq} Hamiltonian. Physically this Hamiltonian represent the interaction of the strongly correlated itinerant electrons with the background spin textures. We rederived this theory in Appendix A for convenience of the readers.

The resulting Hamiltonian (A17) is applicable to any 2D lattice structure and spin texture provided: (i) correlation between electrons should be strong enough to exclude doubly occupied sites and (ii) the coupling between itinerant electrons and local moments is strong. KLM in the strong Kondo coupling regime satisfies these conditions [48,49]. As KLM and periodic Anderson model (PAM) are related, these conditions are satisfied for PAM with strong onsite Coulomb repulsion of f electrons and strong hybridization between localized f electrons and conduction s electrons. Compounds having heavy fermion elements are likely to satisfy these conditions [50–52]. In fact in some VdW compounds, the signs of KLM have been predicted [35,53,54].

A. Hamiltonian on a bipartite lattice

We investigate the Hamiltonian (A17) on a honeycomb bipartite ($L = A \oplus B$; A and B are sublattices) lattice with spin texture given in Eq. (1). In L the nearest neighbor (NN) hopping is related to the hopping from one sublattice to the another ($A \rightarrow B$, $B \rightarrow A$), and the next nearest neighbor (NNN) hopping is related to the hopping on the same sublattices ($A \rightarrow A$, $B \rightarrow B$). On a honeycomb lattice the NN (a_n), and

NNN (b_n) lattice vectors are [see Fig. 3(a)]

$$\vec{a}_1 = \left(\frac{\sqrt{3}}{2}, \frac{1}{2}\right), \qquad \vec{a}_2 = \left(-\frac{\sqrt{3}}{2}, \frac{1}{2}\right), \quad \vec{a}_3 = (0, -1),$$

$$\vec{b}_1 = \left(-\frac{\sqrt{3}}{2}, \frac{3}{2}\right), \quad \vec{b}_2 = \left(-\frac{\sqrt{3}}{2}, -\frac{3}{2}\right), \quad \vec{b}_3 = (\sqrt{3}, 0).$$

Here we have assumed a constant unit lattice. In momentum space (see Appendix B),

$$H(\vec{k}) = \sum_{\vec{k}} \bar{\psi}_{\vec{k}} \mathcal{H}(\vec{k}) \psi_{\vec{k}}.$$

The $\psi_{\vec{k}} = [f_{\vec{k},A} \quad f_{\vec{k},B}]^T$ contains the holon creation operators of the $\vec{k}$th momentum on the two sublattice A and B. The single mode kernel is $\mathcal{H}(\vec{k}) = \mathcal{H}_0(\vec{k}) \cdot \mathcal{I} + \mathcal{H}_i(\vec{k}) \cdot \vec{\sigma}_i$. $\mathcal{I}$ is the unit matrix; $\vec{\sigma}_i$ are the Pauli matrices, and $\mathcal{H}_i(\vec{k})$ are the corresponding kernels. Explicitly

$$\mathcal{H}(\vec{k}) = \mathcal{H}_0 \mathcal{I} + \mathcal{H}_x(\vec{k})\sigma_x + \mathcal{H}_y(\vec{k})\sigma_y + \mathcal{H}_z(\vec{k})\sigma_z;$$

$$\mathcal{H}_0 = -2t_2 w_n^S \hat{\mathcal{F}} \left[1 + g_n \cos 2\vec{q}_1 \left(\vec{r}_i + \frac{\vec{b}_n}{2}\right)\right]^S * \left\{\cos S\vec{q}_2\vec{b}_n \cos \vec{k}\vec{b}_n + 2S \sin S\vec{q}_2\vec{b}_n \sum_{\vec{k}'} p(\vec{k}') \cos(\vec{k} + \vec{k}')\vec{b}_n\right\},$$

$$\mathcal{H}_x = +t_1 w_n'^S \hat{\mathcal{F}} \left[1 - g_n' \cos 2\vec{q}_1 \left(\vec{r}_i + \frac{\vec{a}_n}{2}\right)\right]^S * \cos \vec{k}\vec{a}_n, \tag{2}$$

$$\mathcal{H}_y = +t_1 w_n'^S \hat{\mathcal{F}} \left[1 - g_n' \cos 2\vec{q}_1 \left(\vec{r}_i + \frac{\vec{a}_n}{2}\right)\right]^S * \sin \vec{k}\vec{a}_n,$$

$$\mathcal{H}_z = -2t_2 w_n^S \hat{\mathcal{F}} \left[1 + g_n \cos 2\vec{q}_1 \left(\vec{r}_i + \frac{\vec{b}_n}{2}\right)\right]^S * \left\{-\sin S\vec{q}_2\vec{b}_n \sin \vec{k}\vec{b}_n + 2S \cos S\vec{q}_2\vec{b}_n \sum_{\vec{k}'} p(\vec{k}') \sin(\vec{k} + \vec{k}')\vec{b}_n\right\},$$

where

$$w_n \equiv \frac{1}{2} + \left(\frac{1}{4} + \frac{\cos \vec{q}_2\vec{b}_n}{4}\right) \cos \vec{q}_1\vec{b}_n; \quad g_n \equiv \left[\left(\frac{1}{4} - \frac{\cos \vec{q}_2\vec{b}_n}{4}\right)\middle/ w_n\right];$$

$$w_n' \equiv \frac{1}{2} - \left(\frac{1}{4} + \frac{\cos \vec{q}_2\vec{a}_n}{4}\right) \cos \vec{q}_1\vec{a}_n; \quad g_n' \equiv \left[\left(\frac{1}{4} - \frac{\cos \vec{q}_2\vec{a}_n}{4}\right)\middle/ w_n'\right].$$

Here, t_1 and t_2 are the electron NN and NNN hopping factors, respectively. $p(\vec{k}')$ is the Fourier coefficient of the real space function:

$$p(\vec{r}_i) = \text{atan}\left[\frac{1}{\hbar(\vec{r}_i) \csc \vec{q}_2\vec{b}_n + \cot \vec{q}_2\vec{b}_n}\right] = \sum_{k'} p(\vec{k}')e^{-i\vec{k}'\vec{r}_i},$$

where

$$\hbar(\vec{r}_i) \equiv \frac{2 + \cos \vec{q}_1\vec{b}_n + \left[4\cos \frac{\vec{q}_1\vec{b}_n}{2} + 1\right] \cos 2\vec{q}_1\left(\vec{r}_i + \frac{\vec{b}_n}{2}\right)}{\cos \vec{q}_1\vec{b}_n - \cos 2\vec{q}_1\left(\vec{r}_i + \frac{\vec{b}_n}{2}\right)}. \tag{3}$$

The $p(\vec{k}')$ is a function of $\vec{q}_1$ and $\vec{q}_2$. In Figs. 3(c)–3(e), we plot $p(\vec{r}_i)$ and corresponding $p(\vec{k}')$ for different combinations of $\vec{q}_1$ and $\vec{q}_2$. We observe that $p(\vec{k}') \ll 1$ for whole range of $\vec{k}'$; it is true irrespective of $\vec{q}_1$ and $\vec{q}_2$.

In Fig. 3(b), we plotted w_n, w_n', g_n, and g_n' for $\vec{q}_1 = (2q_{1x}/\sqrt{3}, 0)$, $\vec{q}_2 = (2q_{2x}/\sqrt{3}, 0)$; where $0 < q_{1x}, q_{2x} < \sqrt{3}\pi/2$. We observe that for whole range of q_{1x} and q_{2x}, these functions are positive and less than unity. As these are even functions of $\vec{q}_1$ and $\vec{q}_2$, the same is true for $-\sqrt{3}\pi/2 < q_{1x}, q_{2x} < 0$. $\hat{\mathcal{F}}$ represents the Fourier transform operator. $\langle\langle*\rangle\rangle$ is the convolution operator.
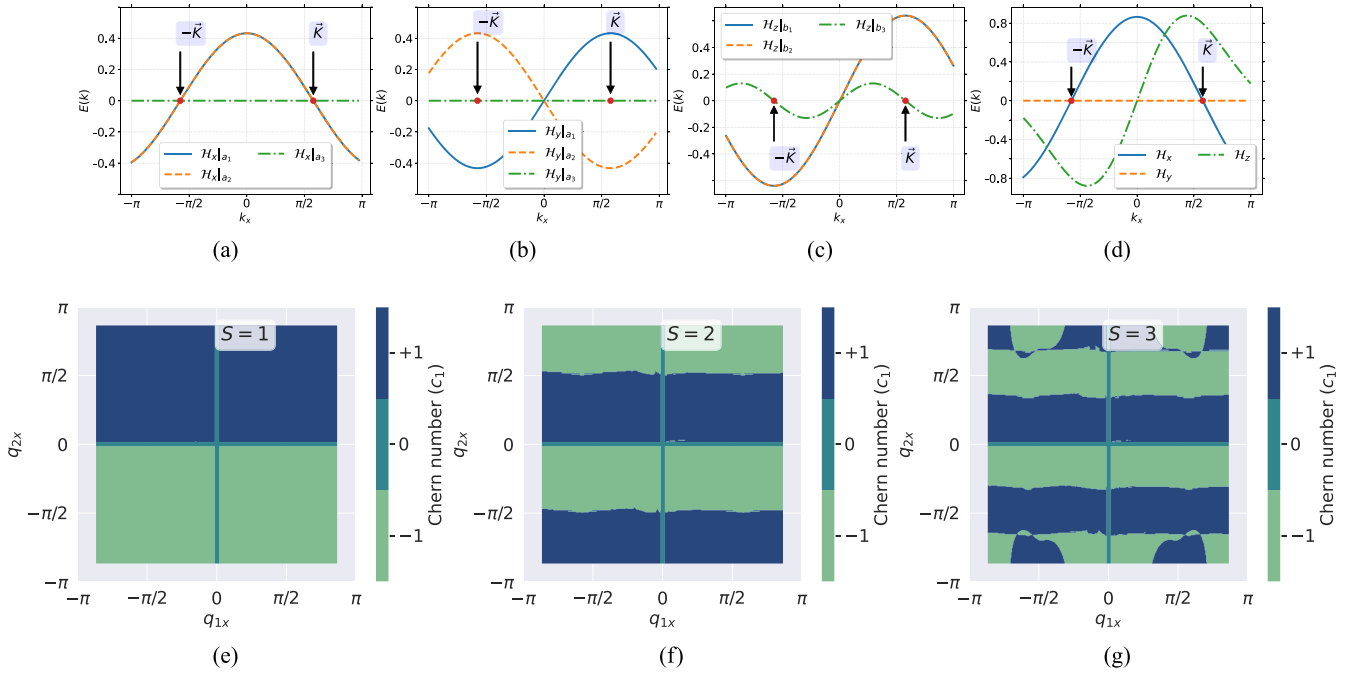
FIG. 4. Dependence of (a) $\mathcal{H}_x$ and (b) $\mathcal{H}_y$ on the momentum vector k_x corresponding to the three NN vectors; the value of $k_y = 0$ everywhere. We have taken $\vec{q}_1 = (\pi/4, 0)$ and $\vec{q}_2 = (\pi/4, 0)$. The coordinate of $\pm\vec{K} = (\pm\pi/\sqrt{3}, 0)$. (c) The same dependence of $\mathcal{H}_z$ on corresponding NNN vectors. (d) Summation of the previously plotted three components of the $\mathcal{H}_x$, $\mathcal{H}_y$, and $\mathcal{H}_z$. [(e)–(g)] Chern number dependence on q_{1x} and q_{2x} for $S = 1, 2,$ and 3 calculated using Eqs. (6)–(8), respectively.

S is the effective spin of the magnetic atoms. In the following sections, the Chern number for integer and half-integer spins are discussed.

B. Chern number for spin $S = 1$

The Hamiltonian for integer spin $S = 1$ is found from Eq. (2):

$$\mathcal{H}_0 = -2t_2 \sum_n w_n \left[1 + \frac{g_n}{2}\cos 2\vec{q}_1\vec{b}_n\right]\left\{\cos\vec{q}_2\vec{b}_n\cos\vec{k}\vec{b}_n + 2\sin\vec{q}_2\vec{b}_n\sum_{\vec{k}'}p(\vec{k}')\cos(\vec{k}+\vec{k}')\vec{b}_n\right\},$$

$$\mathcal{H}_x = +t_1 \sum_n w_n'\left[1 - \frac{g_n'}{2}\cos 2\vec{q}_1\vec{a}_n\right] \times \cos\vec{k}\vec{a}_n,$$

$$\mathcal{H}_y = +t_1 \sum_n w_n'\left[1 - \frac{g_n'}{2}\cos 2\vec{q}_1\vec{a}_n\right] \times \sin\vec{k}\vec{a}_n,$$

$$\mathcal{H}_z = -2t_2 \sum_n w_n \left[1 + \frac{g_n}{2}\cos 2\vec{q}_1\vec{b}_n\right]\left\{-\sin\vec{q}_2\vec{b}_n\sin\vec{k}\vec{b}_n + 2\cos\vec{q}_2\vec{b}_n\sum_{\vec{k}'}p(\vec{k}')\sin(\vec{k}+\vec{k}')\vec{b}_n\right\}. \quad (4)$$

For topological properties to appear the condition $\mathcal{H}_x = \mathcal{H}_y = 0$ and $\mathcal{H}_z \neq 0$ should be satisfied simultaneously (see Sec. 3.5.6 of Ref. [55]). If we take $\vec{q}_1 = (2q_{1x}/\sqrt{3}, 0)$ and $\vec{q}_2 = (2q_{2x}/\sqrt{3}, 0)$, where $-\sqrt{3}\pi/2 < q_{1x}$, $q_{2x} < \sqrt{3}\pi/2$, then at the point $\pm\vec{K} = (\pm\pi/\sqrt{3}, 0)$ this condition is satisfied (see Appendix F). To show this in Figs. 4(a)–4(c), we have plotted the $\mathcal{H}_x$, $\mathcal{H}_y$, and $\mathcal{H}_z$ for $\vec{q}_1 = (\pi/4, 0)$ and $\vec{q}_2 = (\pi/4, 0)$. We observe that at $\pm\vec{K}$ all three components of $\mathcal{H}_x$ are zero. For $\mathcal{H}_y$ at $\pm\vec{K}$, the $\vec{a}_3$ component is zero, and

the $\vec{a}_1$ and $\vec{a}_2$ components are of opposite sign. In result the sum of the all three components of $\mathcal{H}_y$ is zero at $\pm\vec{K}$. For $\mathcal{H}_z$, the $\vec{b}_3$ component is zero at $\pm\vec{K}$, however, the $\vec{b}_1$ and $\vec{b}_2$ components are nonzero. Therefore the aforementioned topological condition is satisfied.

We note that the topological property for $\vec{q}_1 = (2q_{1x}/\sqrt{3}, 0)$ and $\vec{q}_2 = (2q_{2x}/\sqrt{3}, 0)$ is defined by either the $\vec{b}_1$ or the $\vec{b}_2$ component of $\mathcal{H}_z$ as (i) only they have nonzero values at $\pm\vec{K}$, (ii) both of them are identical to each

other. Considering only $\vec{b}_1$ component, the Chern number is

$$c_1 = \frac{\text{sgn}[\mathcal{H}_z|_{\vec{b}_1}(\vec{K})] - \text{sgn}[\mathcal{H}_z|_{\vec{b}_1}(-\vec{K})]}{2}. \quad (5)$$

Using Eq. (5) in Eq. (4), we will get

$$c_1 = \text{sgn}\left\{ \sin q_{2x} - 2\cos q_{2x} \sum_{\vec{k}'} \mathcal{p}(\vec{k}') \sin\left(\frac{\pi}{2} + \vec{k}'\vec{b}_1\right) \right\};$$

$$\text{where} \quad -\frac{\sqrt{3}\pi}{2} \leqslant q_{1x} \leqslant \frac{\sqrt{3}\pi}{2}, -\frac{\sqrt{3}\pi}{2} \leqslant q_{2x} \leqslant \frac{\sqrt{3}\pi}{2}. \quad (6)$$

The $\vec{q}_1$ dependence of c_1 enters through $\mathcal{p}(\vec{k}')$, however, as $\mathcal{p}(\vec{k}') \ll 1$ we expect a very weak dependence. In Fig. 4(e), we plot the dependence of c_1 on q_{1x} and q_{2x}; as was expected $\vec{q}_1$ almost does not have any effect on Chern number.

It is important to note that on a honeycomb lattice, the Chern number is defined only by $\vec{b}_1$ or $\vec{b}_2$ component of the $\mathcal{H}_z$ when following conditions are satisfied: (i) the y components of the spin modulation vectors are zero: $\vec{q}_1 = (2q_{1x}/\sqrt{3}, 0)$ and $\vec{q}_2 = (2q_{2x}/\sqrt{3}, 0)$, and (ii) the Hamiltonian can be represented in the same form as Eq. (4).[3]

C. Chern number for $S = 2$ and 3

For higher spin $S = 2$ and 3, one will expand the terms containing $\mathcal{g}_n$ and $\mathcal{g}_n'$ in Eq. (2). The Hamiltonian for $S = 2$ is given in Eq. (C2). Comparing Eqs. (4) and (C2), we observe that they are analogous to each other, hence, the Chern number will be defined by the $\vec{b}_1$ (or $\vec{b}_2$) component of $\mathcal{H}_z$. The Chern number for $S = 2$ is

$$c_1 = \text{sgn}\left[\left(1 + \frac{g_1^2}{2}\right) + g_1 \cos 2q_{1x} + \frac{g_1^2}{2}\cos 4q_{1x} \right]$$

$$\times \text{sgn}\left[\sin 2q_{2x} - 4\cos 2q_{2x} \sum_{\vec{k}'} \mathcal{p}(\vec{k}') \sin\left(\frac{\pi}{2} + \vec{k}'\vec{b}_n\right) \right]. \quad (7)$$

The dependence of c_1 on q_{1x} and q_{2x} is plotted in Fig. 4(f). We observe very weak dependence of c_1 on q_{1x}.

In Eq. (C3), we give the Hamiltonian for $S = 3$. Equation (C3) is also analogous to the Eq. (4). Hence, as before, the Chern number will be given by $\vec{b}_1$ component

---

of $\mathcal{H}_z$:

$$c_1 = \text{sgn}\left[\begin{array}{c} \left(1 + \frac{3g_1^2}{2}\right) + \left(3\mathcal{g}_1 + \frac{3g_1^3}{4}\right)\cos 2q_{1x} \\ -\frac{3g_1^2}{2}\cos 4q_{1x} - \frac{g_1^3}{4}\cos 6q_{1x} \end{array} \right]$$

$$\times \text{sgn}\left[\sin 3q_{2x} - 6\cos 3q_{2x} \sum_{\vec{k}'} \mathcal{p}(\vec{k}') \sin\left(\frac{\pi}{2} + \vec{k}'\vec{b}_n\right) \right]. \quad (8)$$

In Fig. 4(g), we plot the dependence of c_1 on q_{1x} and q_{2x}. Here, in comparison to Figs. 4(e) and 4(f), the dependence of c_1 on q_{1x} increases; it can be clearly seen in the vicinity of $q_{1x} \approx \pm\pi/2$, $\pi/2 < q_{2x} < \sqrt{3}\pi/2$. For other values of q_{1x} and q_{2x}, the dependence is very weak.

D. Chern number for $S = 1/2$ and $3/2$

Finding a closed analytical expression of Chern number for $S = 1/2$ is not possible, as Fourier transform of the terms

$$\left[1 - \mathcal{g}_n' \cos 2\vec{q}_1\left(\vec{r}_i + \frac{\vec{a}_n}{2}\right) \right]^{1/2},$$

$$\left[1 + \mathcal{g}_n \cos 2\vec{q}_1\left(\vec{r}_i + \frac{\vec{b}_n}{2}\right) \right]^{1/2}, \quad (9)$$

are not available. One can find the Hamiltonian in the limiting cases of $\mathcal{g}_n$ and $\mathcal{g}_n'$. We can have four combinations of limiting cases: (i) $\mathcal{g}_n \ll 1$, $\mathcal{g}_n' \ll 1$, (ii) $\mathcal{g}_n \ll 1$, $\mathcal{g}_n' \lessapprox 1$, (iii) $\mathcal{g}_n \lessapprox 1$, $\mathcal{g}_n' \ll 1$, and (iv) $\mathcal{g}_n \lessapprox 1$, $\mathcal{g}_n' \lessapprox 1$. In Fig. 5(a), we showed the values of q_{1x} and q_{2x} for which these limiting cases are applicable; we assumed here threshold of 0.2, i.e., four different combinations of $0 < \mathcal{g}_1$, $\mathcal{g}_1' \leqslant 0.2$ and $0.8 \leqslant \mathcal{g}_1$, $\mathcal{g}_1' \leqslant 1$. In Fig. 5(a), we observe that only the combinations $\mathcal{g}_1' \ll 1$, $\mathcal{g}_1 \ll 1$ and $\mathcal{g}_1' \lessapprox 1$, $\mathcal{g}_1 \ll 1$ are prominent, hence we analyze only these two combinations. The Hamiltonian for $\mathcal{g}_1' \ll 1$, $\mathcal{g}_1 \ll 1$ is given in Eq. (D3) and for $\mathcal{g}_1' \lessapprox 1$, $\mathcal{g}_1 \ll 1$ is given in Eq. (D7). Both these Hamiltonians are analogous to the Eq. (4). Besides, the $\mathcal{H}_z$ for both these Hamiltonians is the same as it corresponds to the single case $\mathcal{g}_1 \ll 1$. Hence, the expression for the Chern number will be same:

$$c_1 = \text{sgn}\left[\sin\frac{q_{2x}}{2} - \cos\frac{q_{2x}}{2} \sum_{\vec{k}'} \mathcal{p}(\vec{k}') \sin\left(\frac{\pi}{2} + \vec{k}'\vec{b}_1\right) \right]. \quad (10)$$

In Fig. 5(b), we plot the Chern number for $S = 1/2$.

For $S = 3/2$, the Chern number is also found analogously. The idea is to represent the functions containing $\mathcal{g}_n$ in Eq. (4) as a multiplication of powers of 1 and $1/2$, then to apply the above discussed limiting conditions to find the corresponding Hamiltonian and Chern number. The Hamiltonians corresponding to the two combinations are given in Eq. (E2) ($\mathcal{g}_1' \ll 1$, $\mathcal{g}_1 \ll 1$) and (E3) ($\mathcal{g}_1' \lessapprox 1$, $\mathcal{g}_1 \ll 1$). The Chern

---

[3]By same form as Eq. (4) we meant that $\mathcal{H}_x$ ($\mathcal{H}_y$) is multiplication of $\cos \vec{k}\vec{a}_n$ ($\sin \vec{k}\vec{a}_n$) and an even function (with respect to $\vec{q}_1$ and $\vec{q}_2$). In case of $\mathcal{H}_x$ and $\mathcal{H}_y$, the function $w_n'(1 - \mathcal{g}_n'/2\cos 2\vec{q}_1\vec{a}_n)$ is even; the evenness of $\mathcal{g}_n$, $\mathcal{g}_n'$, w_n, and w_n' can be observed in Eq. (2) as they are a function of cosine. Multiplication of $\mathcal{H}_x$ ($\mathcal{H}_y$) by $\cos \vec{k}a_n$ ($\cos \vec{k}a_n$) allow us to make $\mathcal{H}_x = 0$ ($\mathcal{H}_y = 0$) at $\pm K$. For explicit explanation and derivation of this point, please refer Appendix F.

FIG. 5. (a) Values of q_{1x} and q_{2x} where four different combinations of limiting cases of $\mathscr{g}_1$ and $\mathscr{g}_1'$ are applicable. We assumed the threshold of of 0.2, i.e., different combinations of $0 < \mathscr{g}_1$, $\mathscr{g}_1' \leqslant 0.2$ and $0.8 \leqslant \mathscr{g}_1$, $\mathscr{g}_1' \leqslant 1$. [(b) and (c)] Chern number dependence on q_{1x} and q_{2x} for $S = 1/2$ and 3/2 calculated from Eqs. (10) and (11), respectively.

number is

$$
c_1 = \text{sgn}\left[\left(1 + \frac{\mathscr{g}_1'^2}{4} \right) + \frac{3}{2}\mathscr{g}_1 \cos 2q_{1x} + \frac{\mathscr{g}_1'^2}{4}\cos q_{1x} \right]
$$

$$
\times \text{sgn}\left[\sin \frac{3q_{2x}}{2} - 3\cos \frac{3q_{2x}}{2} \sum_{\vec{k}'} \mathscr{p}(\vec{k}') \sin\left(\frac{\pi}{2} + |\vec{k}'\vec{b}_1| \right) \right],
$$

(11)

In Fig. 5(c), we plot the Chern number dependence on q_{1x} and q_{2x} for $S = 3/2$. In Fig. 5(d), we showed the Chern number for 5/2; the explicit expression is not shown here, but it is calculated using the same procedure, representing the function containing $\mathscr{g}_n$ and $\mathscr{g}_n'$ in Eq. (4) as a multiplication of powers of 2 and 1/2.

III. DISCUSSION

In Table I, we summarize the results from the previous section. From the dependence of the Chern number on q_{1x} and q_{2x} for integer spin [Figs. 4(e)–4(g)], it can be observed that the Chern number changes multiple times in the range $0 < q_{1x}, q_{2x} < \sqrt{3}\pi/2$ only for higher integer spins $S > 2$. Hence experimentally the change in the direction of the topological Hall resistivity ρ_{xy}^{THE} (it is proportional to the c_1) can only be observed at higher spin $S > 2$.

When c_1 for the half-integer spin (apart from $S = 1/2$) is compared with the c_1 for the corresponding floor integer spin ($\lfloor S \rfloor$), i.e., c_1 for $S = 3/2$ [Fig. 5(c)] with $S = 1$ [Fig. 4(e)] or for $S = 5/2$ [Fig. 5(d)] with $S = 2$ [Fig. 4(f)], we see that they are identical to each other in the regions where $\mathscr{g}_1' \ll 1$, $\mathscr{g}_1 \ll 1$ and $\mathscr{g}_1' \lessapprox 1$, $\mathscr{g}_1 \ll 1$ are satisfied. We can assume that the effect of the functions containing $\mathscr{g}_n$ with $S = 1/2$ is

very weak. Hence, only the integer components of the half-integer spins have effects on c_1. For example, for $S = 9/2 = 4 + (1/2)$, the dependence of c_1 on q_{1x} and q_{2x} will be same as $S = 4$; c_1 for $S = 4$ can be found exactly. However, whether this assumption is true can only be probed experimentally.

In Figs. 4(e)–4(g) and 5(b)–5(d), we observe that $c_1 = 0$ when $q_{1x} = 0$ or $q_{2x} = 0$. Physically $q_{1x} = 0$ means ferromagnetic (FM) phase. Observing Eq. (A17), we can conclude that the Hamiltonian represents an effective spinless electronic system in the FM case. Whether the system is insulator or metal depends on the initial parameters (t_{ij}, μ). $q_{2x} = 0$ means rotation of the spin texture only on yz plane (coplanar); whether the system is insulator or metal depends on q_{1x}. For both FM and copolanar cases, the system does not have THE [56].

A. Closing of a band gap

From the band structure point of view, the $\pm\sqrt{\mathcal{H}_x^2 + \mathcal{H}_y^2 + \mathcal{H}_z^2}$ represent the valence $(-)$ and conduction $(+)$ bands; we have dropped $\mathcal{H}_0$ as it is just an additive term, which can always be subtracted out. The band gap closes at $\pm\vec{K}$ when $\mathcal{H}_z = 0$. As $\mathcal{H}_z$ is a function of q_{1x} and q_{2x}, at some of their specific values the gap closes. In Fig. 6, we show the gap closing for $S = 2$ for $q_{1x} = \pi/4$, $q_{2x} = 1.81$, $k_y = 0$.
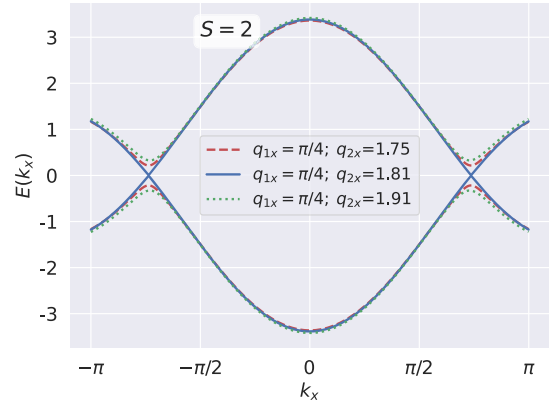

FIG. 6. Dependence of energy $E(k_x) = \pm\sqrt{\mathcal{H}_x^2 + \mathcal{H}_y^2 + \mathcal{H}_z^2}$ on $k_x \in (-\pi, +\pi)$ for the same $q_{1x} = \pi/4$ and different q_{2x}. We have taken $S = 2$, $k_y = 0$. The complete Hamiltonian is given in Eq. (C2). The gap closes at $\pm\vec{K} = (\pm\pi/\sqrt{3}, 0)$ for $q_{2x} = 1.81$.

TABLE I. Expressions for Hamiltonian, Chern number, and figures of the Chern number dependence on q_{1x}, q_{2x} and for $S = 1/2$, 1, 3/2, 2 and , 3. The Hamiltonians for $S = 1/2$ and 3/2 correspond to two cases (i) $\mathscr{g}_1' \ll 1$, $\mathscr{g}_1 \ll 1$ and (ii) $\mathscr{g}_1' \lessapprox 1$, $\mathscr{g}_1 \ll 1$.

	$S = 1/2$	$S = 1$	$S = 3/2$	$S = 2$	$S = 3$
Hamiltonian	(D3), (D7)	(4)	(E2), (E3)	(C2)	(C3)
Chern Num. (Eq.)	(10)	(6)	(11)	(7)	(8)
Chern Num. (Fig.)	5(b)	4(e)	5(c)	4(f)	4(g)

Every time there is a change of c_1 the band gap closes and reopens. Hence, for higher spins, the gap closes and reopens multiple times as q_{1x} and q_{2x} are modulated.

B. Comparison with th Haldane model

In the Haldane model [57], the topological property was controlled by the sublattice onsite potential (M) and the constant phase accumulation of electrons due to NNN hopping (defined as ϕ in Ref. [57]). The total accumulated phase due to a closed path on the lattice was interpreted as effective

(fictitious) magnetic field. In our case, the phase due to NNN hopping is [see Eq. (B7)]

$$\phi_n = S\left[2\,\mathrm{atan}\left[\frac{1}{\hbar(\vec{r}_i)\csc \vec{q}_2\vec{b}_n + \cot \vec{q}_2\vec{b}_n}\right] - \vec{q}_2\vec{b}_n\right]. \quad (12)$$

Hence, now the effective magnetic field in a closed loop is function of S, $\vec{q}_1$, and $\vec{q}_2$. In fact, we can insert phenomenological sublattice potential M into the $\mathcal{H}_z$ of Eq. (2). The Chern number for $S = 1$ in the presence of M can be found using Eqs. (5) and (4):

$$
c_1 = \frac{\mathrm{sgn}\left\{M - \left[\begin{array}{c} 4t_2 w_1\left(1 + \frac{g_1}{2}\cos 2\vec{q}_{1x}\vec{b}_n\right) \\ \times \left[\sin q_{2x} - 2\cos q_{2x}\sum_{\vec{k}'}\wp(\vec{k}')\sin\left(\frac{\pi}{2} + \vec{k}'\vec{b}_1\right)\right]\end{array}\right]\right\}}{2}
$$

$$
= -\frac{\mathrm{sgn}\left\{M + \left[\begin{array}{c} 4t_2 w_1\left(1 + \frac{g_1}{2}\cos 2\vec{q}_{1x}\vec{b}_n\right) \\ \times \left[\sin q_{2x} - 2\cos q_{2x}\sum_{\vec{k}'}\wp(\vec{k}')\sin\left(\frac{\pi}{2} + \vec{k}'\vec{b}_1\right)\right]\end{array}\right]\right\}}{2}. \quad (13)
$$

Notice that now the c_1 depends on M and the prefactor containing g_1 and w_1; which was absent in Eq. (6). The same procedure can be used to find Chern number for $S = 2$ and $S = 3$. For a half-integer spin, the Chern number can be found only in the limited regions of q_{1x}—q_{2x} phase space [Fig. 5(a)]. In Fig. 7, we plotted the Chern number dependence on M/t_2 and q_{2x} for $S = 1,\ 2,\ 3$; the $q_{1x} = \pi/4$ is kept constant.

C. Minimum energy

To understand the thermodynamics, we calculate the total internal energy of the system (U_{internal}), which can be found by integrating the lower band energy over the whole Brillouin zone. In Fig. 8, we plotted the U_{internal} for different S. For all the cases, the lowest energy has an antiferromagnetic (AFM) configuration $\vec{q}_1 = (\pm\pi, 0)$. Away from the lowest

energy, equal energy contours appear in q_{1x}-q_{2x} phase space, meaning, several degenerate spin configurations for a given energy. Interestingly, for $S = 1$, every equal energy contour ends at an AFM (or $q_{2x} = \sqrt{3}\pi/2$) configuration; in other words, all are open contours. However, for $S = 2$ and 3, the closed contours appear that do not include in the AFM (or $q_{2x} = \sqrt{3}\pi/2$) state.

D. Perspective materials for the application of the model

One of the perspective materials for observing the aforementioned effect is $\mathrm{Fe}_{N=3,4,5}\mathrm{GeTe}_2$ [58]. In Fig. 9, we showed the lattice structures of F3GT and $\mathrm{Fe}_4\mathrm{GeTe}_2$ (F4GT). They belong to vdW materials, where usually the magnetic layers
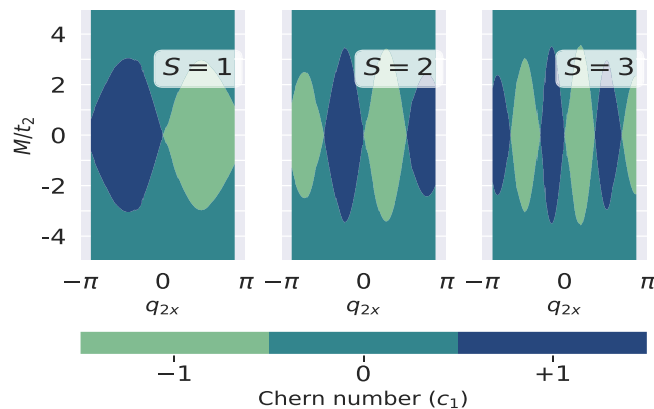

FIG. 7. Chern number dependence on the sublattice potential M/t_2 and q_{2x} for $S = 1,\ 2,\ 3$; we keep $q_{1x} = \pi/4$ constant.
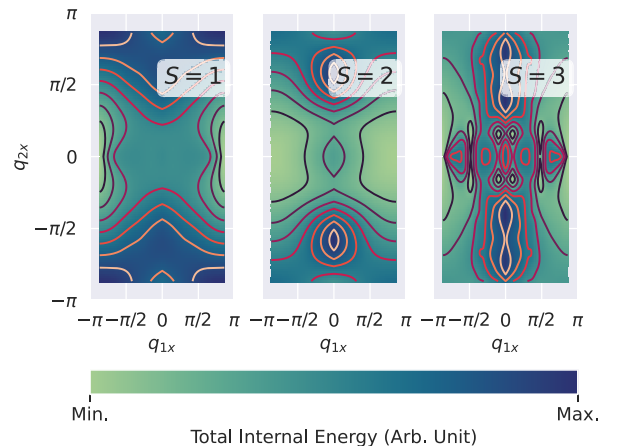

FIG. 8. Dependence of the total internal energy on the wave vectors q_{1x} and q_{2x}. The lines represent the equal energy contours.
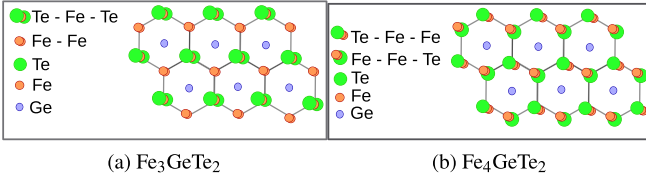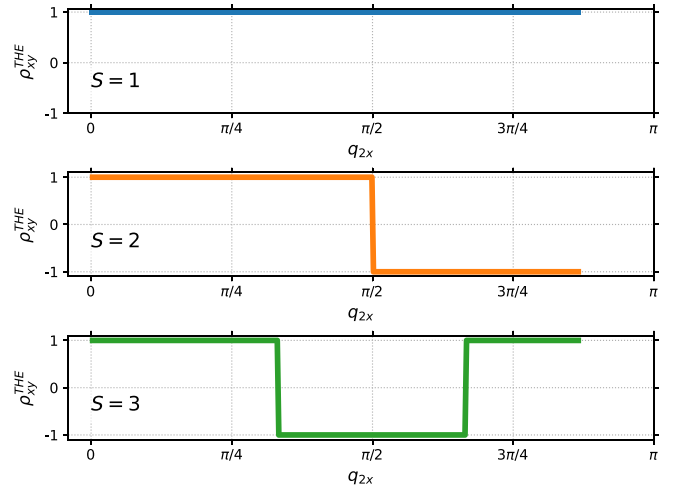
(a) Fe₃GeTe₂

(b) Fe₄GeTe₂

FIG. 9. Effective magnetic bipartite honeycomb lattice.

FIG. 10. Dependence of the topological Hall resistivity ρ_{xy}^{THE} on the azimuthal spin modulation vector q_{2x}. The ρ_{xy}^{THE} is represented in units of $e^2/2\pi\hbar$. The polar angle $q_{1x} = \pi/4$ is kept constant.

are sandwiched in between the nonmagnetic layer in different configurations. For example, in F3GT, a single Fe-Fe dumbbell and a single Fe atom are placed alternatively in a honeycomb lattice pattern; at the center of the honeycomb lattice, the single Ge atom is placed [59,60]. This whole structure containing the Fe and Ge atoms are sandwiched in between Te atoms. The F4GT has the same honeycomb lattice structure, however, now instead of a single dumbbell, two dumbbells of Fe atoms are present; the single Fe atoms are absent [59,60]. Both F3GT and F4GT can be treated as effective bipartite lattices. In F3GT, the Fe-Fe dumbbell and Fe atoms correspond to the two sublattices of the bipartite lattice. For F4GT, the bonding between Fe-Fe dumbbell and Te atoms creates an effective bipartite lattice, i.e., one of the sublattice contains the dumbbell with the upper Fe atom of the dumbbell bonded to the Te atom, and the other sublattice contains the lower Fe atom of the dumbbell bonded to the Te atom.

The discussed spin texture in this paper had already been observed in these materials [32]. Fundamental requirements of the proposed model is the presence of localized angular momentum (spin S), strong correlation between conduction electrons, strong coupling between conduction electrons, and localized angular momentum (KLM in strong coupling limit have all these properties). In F3GT, the electron correlation is around $U = 5$ to 5.5 eV [29,30], which is comparable to the $U = 6.2$ eV for the prototypical heavy fermion compound CeIn₃. For F4GT, also strong electronic correlation was predicted from numerical calculations [61]. The localized nature of angular momentum for F3GT ($S = 3$) and F4GT ($S = 7/2$) has been predicted [59,60,62,63]. Besides, the Kondo lattice behavior was also predicted in F3GT [35] and F4GT [64]. Hence at low temperatures ($T \sim T_K$; T_K is the Kondo temperature), our model can be applied in these materials, as Kondo coupling is strong near T_K [65]. In the following sections, we propose several heterostructures to control the spin modulating vectors in F3GT and F4GT.

E. Experiment

Naturally, the question arises how the above effect can be physically verified? One of the indirect way of confirming this effect is through the Hall resistivity measurement. The topological Hall resistivity is proportional to the Chern number [66], $\rho_{xy}^{\text{THE}} = -\sigma_{xy}/(\sigma_{xy}^2 + \sigma_{xx}^2)$ here $\sigma_{xy} = e^2 c_1/(2\pi\hbar)$. Consequently, as the $\pm c_1$ depends on q_{1x}, q_{2x} we will observe the change in direction of ρ_{xy}^{THE} with changing q_{1x}, q_{2x}. In Fig. 10, we plotted the dependence of ρ_{xy}^{THE} on the azimuthal angle q_{2x}, while keeping $q_{1x} = \pi/4$ constant. One can observe that for

$S = 1$, there is no change in the sign of the ρ_{xy}^{THE}, hence, the predicted effect in this case is not possible to detect. However, for higher $S = 2$ and 3, there are multiple sign change with increasing q_{2x}. Therefore materials with high magnetic moments (F3GT, F4GT) are good experimental platforms to observe this effect. Now the question arises: how one can control the vector q_{2x} in F3GT (or F4GT)? References [36,67,68] showed that the density of magnetic stripes (therefore q_{2x}) can be controlled by tuning the temperature and external magnetic field. Thickness [38] and defect [69,70] engineering can also be used to manipulate topological spin configurations.

Another idea to control q_{2x} is to use heterostructures [71–73] of F3GT or F4GT with two perpendicular DMI vectors: (i) bulk DMI and (ii) interfacial DMI. The bulk DMI arises due to intrinsic broken bulk inversion symmetry ($r \to -r$). It can be broken through stoichiometry engineering [69,70], strain, or electric field [74,75]. The interfacial DMI occurs due to cosmetically broken mirror symmetry ($z \to -z$) at the interface of the heterostructures [76,77]. The structure specific bulk DMI is hard to control, however, the interfacial DMI can be controlled by the extrinsic means [78–82]. Therefore a heterostructure can be synthesized where an F3GT or F4GT layer is placed over a substrate; for a substrate, one can use materials with strong spin-orbit coupling, where the electrical control of DMI is possible [83].

IV. CONCLUSION

In this work, we analyzed the topological properties of the electronic bands coupled to the background spin texture (1) on a honeycomb lattice for strongly correlated materials. The model is applicable to the materials showing the Kondo lattice behavior in the strong Kondo coupling regime. The explicit expression of Chern number for $S = 1$, 2, 3 is found. We predict that for $S = 1$, 2, 3, the Chern number depends strongly on the azimuthal angle of the spin texture and on the spin of the magnetic atoms S but weakly on polar spin modulation

vector. The Chern number for $S = 1/2$ and $3/2$ is also found, albeit in limiting cases. It is observed that Chern number for these half-integer cases are identical to their floor integer $\lfloor S \rfloor$ (this is not applicable for $S = 1/2$). It is argued that the iron based van der Waals magnets $Fe_{N=3,4,5}GeTe_2$ are suitable materials to observe this effect; these several heterostructures are proposed for experiment. The main physical effect of the result is that for $S > 2$, the topological Hall resistivity changes direction as the wave vectors are modulated. Our method can be applied to find the Chern numbers analytically and exactly for an arbitrary integer S; and for a half-integer S, the Chern number can be found analytically only in limited number of cases.

ACKNOWLEDGMENTS

APPENDIX A: THEORY

We will work in the strong correlation regime in which the underlying Hilbert space is modified as the double occupancy is prohibited. It results in constrained electrons operators which are now isomorphic to the Hubbard operators [84]. Those operators appear as a generators of the $su(2|1)$ superalgebras. As a result charge and spin degrees of freedom can be represented as product of the $SU(2|1)$ supergroup. This is applicable for particles described by the $S = 1/2$, however, for arbitrary spin $S > 1/2$, one will use the $su(2)$ algebra. In the SU(2) formalism, the required theory is constructed under the condition that the background spin field affects the fermion hopping without breaking the global symmetry. The su(2) coherent states (CS) have these properties, as the electron hopping factor is affected only due to CS overlap factors [85,86]. In condensed matter, it is analogous to the Peierls phase factor generated in an external magnetic field. It is the vector potential generated by the noncollinear chiral spin textures [56]. Physically it can be thought of fictitious magnetic field through a plaquette. In field theory, it is the same as the emergent artificial gauge field generated by the U(1) local connection one-form of the spin U(1) complex line bundle. It provides a covariant (geometric) quantization of a spin [87]. In this approach, the underlying base space appears as a classical spin phase space. It is a 2-sphere S^2, which can be mapped to a complex projective space CP^1, endowed with a set of local coordinates $(z, \bar{z})$. In this case, the quantum spin is represented as the section $|z\rangle$ of the principle (monopole) line bundle $P(CP^1, U(1))$. The local connection of the bundle is $a^{(0)} = i\langle z|d|z\rangle$; d is the exterior derivative.

Physically, we start from the lattice KLM:

$$H = -\sum_{ij\sigma}[t_{ij} + J\,S(S+1)\,\delta_{ij}]c_{i\sigma}^\dagger c_{j\sigma}$$

$$+ J\sum_i \hat{\mathbf{S}}_i \cdot (c_{i\sigma}^\dagger \vec{\sigma}_{\sigma\sigma'} c_{i\sigma'}). \quad \text{(A1)}$$

Here $c_{i\sigma}^\dagger$ ($c_{i\sigma}$) is the electron creation (annihilation) operator with the spin σ on site i; $J > 0$ is the exchange coupling constant; $\vec{\sigma}$ is the vector of the *Pauli* spin matrices; $\hat{\mathbf{S}}_i$ is the nuclear spin operator at ith site. The extra J-dependent term $J\,S(S+1)\,\delta_{ij}$ introduced in the hopping parameter is to make sure a finite $J \to \infty$ limit [44]. Under the mean-field approximation, one can represent the nuclear spin operator as product of the localized spin magnitude (S) and their direction ($\vec{n}_i$): $\langle \hat{\mathbf{S}}_i \rangle = S \cdot \vec{n}_i$. In the large Kondo limit $J \to \infty$, the Hubbard model goes into the $U \to \infty$ limit (strongly correlated electronic system) [44]:

$$H \approx -\sum_{i,j,\sigma} t_{ij}\bar{c}_{i\sigma}^\dagger \bar{c}_{j\sigma}. \quad \text{(A2)}$$

Here $\bar{c}_{i\sigma} = c_{i\sigma}(1 - n_{i\bar{\sigma}})$ is the constrained electron operator; $n_{i\bar{\sigma}} = c_{i\bar{\sigma}}^\dagger c_{i\bar{\sigma}}$ is the number operator of the complementary spin. The constraint operator as explained above can be dynamically factorized into the spinless charge fermionic field f_i (holons) and spinfull bosonic z_i fields (spinons) [31,45]. It can be seen that as long as the fermionic field satisfy the condition $f_i^2 \equiv 0$, the local no double occupancy of strongly correlated electron is satisfied rigorously. Here, the holons acquire the band structure of their own; it is the usual behavior for fractionalized electrons [88]. The spinons are handled by mean-field treatment.

The necessary theory was given by the authors recently [31], hence, here we briefly derive the required Hamiltonian. The high-spin CS theory is constructed from the fundamental $S = 1/2$ representation:

$$|z\rangle = (1 + |z|^2)^{-S} e^{z\hat{S}^-}|S\rangle. \quad \text{(A3)}$$

Here $|S\rangle$ is the highest spin-S $su(2)$ state; $\hat{S}^-$ is the spin lowering operator. The S-dependent partition function will be

$$Z = \int D\mu(z, f)\ \exp\mathcal{A}. \quad \text{(A4)}$$

The measure $D\mu(z, f)$ is

$$D\mu(z, f) = \prod_{i,t} \frac{S}{\pi i} \frac{d\bar{z}_i(t)dz_i(t)}{(1 + |z_i|^2)^2} d\bar{f}_i(t)df_i(t). \quad \text{(A5)}$$

Here z_i keeps track of the spin and complex, while f_i keeps track of charge and is a *Grassman* variable. The effective action $\mathcal{A}$ is defined as

$$\mathcal{A} = \sum_i \int_0^\beta \left[ia_i^{(0)} - \bar{f}_i(\partial_t + ia_i^{(0)})f_i\right]dt - \int_0^\beta H\,dt. \quad \text{(A6)}$$

Here, $ia_i^{(0)}$ is the $u(1)$-valued connection one-form of the magnetic monopole bundle as a *spin kinetic* term:

$$ia_i^{(0)} = -\langle z|\partial_t|z\rangle = S\frac{\dot{\bar{z}}z - \bar{z}\dot{z}}{1 + |z|^2}. \quad \text{(A7)}$$

It is analogous to the Berry connection. The Hamiltonian in $\mathcal{A}$ can be written as

$$H = -\sum_{ij} t_{ij}\bar{f}_i f_j e^{ia_{ji}} + \text{H.c.} + \mu\sum_i \bar{f}_i f_i, \quad \text{(A8)}$$

where

$$a_{ij} = -i \ln \langle z_i || z_j \rangle, \quad \langle z_i || z_j \rangle = \frac{(1 + \bar{z}_i z_j)^{2S}}{(1 + |z_j|^2)^S (1 + |z_i|^2)^S}.$$

(A9)

Under a global SU(2) rotation

$$z_i \to \frac{u z_i + v}{-\bar{v} z_i + \bar{u}},$$

(A10)

the phase will be

$$a_i^{(0)} \to a_i^{(0)} - \partial_t \theta_i, \quad a_{ij} \to a_{ij} + \theta_j - \theta_i.$$

(A11)

Here,

$$\theta_i = iS \ln \left(\frac{v \bar{z}_i + u}{\bar{v} z_i + \bar{u}} \right); \quad \begin{bmatrix} u & v \\ -\bar{v} & \bar{u} \end{bmatrix} \in \mathrm{SU}(2).$$

(A12)

The effective action $\mathcal{A}$ remains unchanged under SU(2) transformation of the z_i in conjunction with U(1) transformation of the $f_i \to e^{i\theta_i} f_i$. The real and imaginary parts of the a_{ji} are defined as

$$a_{ji} = \phi_{ji} + i\chi_{ji}; \quad \phi_{ji} = \bar{\phi}_{ji}; \quad \chi_{ji} = \bar{\chi}_{ji}.$$

(A13)

The ϕ_{ji} and χ_{ji} are defined as

$$\phi_{ji} = iS \ln \frac{1 + \bar{z}_i z_j}{1 + \bar{z}_j z_i}$$

$$= iS \ln \frac{(S + S_i^z)(S + S_j^z) + S_i^- S_j^+}{(S + S_i^z)(S + S_j^z) + S_j^- S_i^+},$$

$$\chi_{ji} = -S \ln \frac{(1 + \bar{z}_i z_j)(1 + \bar{z}_j z_i)}{(1 + |z_i|^2)(1 + |z_j|^2)}$$

$$= -S \ln \left(\frac{\vec{S}_i \cdot \vec{S}_j}{2S^2} + \frac{1}{2} \right).$$

(A14)

Here, $\vec{S}_i$ stands for the CS symbols of the $su(2)$ generators [45]. The corresponding values are

$$S_i^z = \frac{1}{2} \frac{1 - |z|^2}{1 + |z|^2}, \quad S_i^+ = \frac{z}{1 + |z|^2}, \quad S_i^- = \frac{\bar{z}}{1 + |z|^2}.$$

(A15)

There is a one-to-one correspondence between the $su(2)$ generators and their CS symbols [47]. Under SU(2) *global* rotation χ_{ji} remains intact, however, ϕ_{ji} transforms as

$$\phi_{ji} \to \phi_{ji} + \theta_i - \theta_j.$$

(A16)

This transformation is analogous to gauge fixing by choosing a specific rotational covariant frame. The dynamical fluxes do not depend on the chosen covariant frame. Substituting Eq. (A14) in the dynamical Hamiltonian (A8), we get

$$H = -\sum_{i,j} t_{ij} \bar{f}_i f_j e^{i\phi_{ji}} \left(\frac{\vec{S}_i \cdot \vec{S}_j}{2S^2} + \frac{1}{2} \right)^S + \mu \sum_i \bar{f}_i f_i.$$

(A17)

Physically, this represents the interaction of the underlying spin field and itinerant spinless fermions.

APPENDIX B: SOLUTION OF HAMILTONIAN ON A BIPARTITE LATTICE

In this section, we use the Hamiltonian (A17) with the spin texture (1) to find the Hamiltonian on a bipartite honeycomb lattice. A bipartite lattice L has two sublattices A and B: $L = A \oplus B$. On a bipartite lattice, the nearest neighbor (NN) hopping corresponds to $A \to B$, and next nearest neighbor (NNN) hopping corresponds to $A \to A$ or $B \to B$. We denote the three NN and NNN honeycomb lattice vectors as $\vec{a}_n$ and $\vec{b}_n$, respectively. The charge and spin degrees of freedom on the A sublattice are f_i and z_i, respectively. For convenience on sublattice B, we can define

$$f_i \to f_i e^{i\theta_i^{(0)}}, \quad z_i \to -\frac{1}{\bar{z}_i}; \quad i \in B.$$

(B1)

Where $\theta_i^{(0)} \equiv \theta_i|_{u=0, v=1}$. Under these transformations, the χ_{ji} from Eq. (A14) remains unchanged, while the $\phi_{ji} \to \phi_{ij} + \theta_j^{(0)} - \theta_i^{(0)}$. This transformation makes the calculation easier, while conserving the form of a_{ij} in Eq. (A11) under *global* SU(2) rotation. The coherent states symbols in Eq. (A15) also changes from $\vec{S}_i \to -\vec{S}_i$.

In a bipartite lattice, the total Hamiltonian will contain three parts depending on hopping of electrons: (i) $A \to A$, (ii) $B \to B$, (iii) $A \to B$. For $A \to A$ ($i, j \in A$) from Eq. (A14) the χ_{ji} is

$$e^{\chi_n} = w_n^S [1 + g_n \cos \vec{q}_1 (2\vec{r}_i + \vec{b}_n)]^S,$$

$$w_n \equiv \frac{1}{2} + \left(\frac{1}{4} + \frac{\cos \vec{q}_2 \vec{b}_n}{4} \right) \cos \vec{q}_1 \vec{b}_n,$$

$$g_n \equiv \left[\left(\frac{1}{4} - \frac{\cos \vec{q}_2 \vec{b}_n}{4} \right) \middle/ w_n \right].$$

(B2)

Here we defined $\vec{b}_n = \vec{r}_j - \vec{r}_i$. It can be easily checked that the values of w_n and g_n are bounded $\in [0, 1]$ and constant for a given $\vec{q}_1$ and $\vec{q}_2$. The ϕ_{ji} is

$$\phi_n = 2S \mathrm{atan} \left[\frac{1}{\hbar(\vec{r}_i) \csc \vec{q}_2 \vec{b}_n + \cot \vec{q}_2 \vec{b}_n} \right];$$

$$\hbar(\vec{r}_i) \equiv \frac{2 + \cos \vec{q}_1 \vec{b}_n + \left[4 \cos \frac{\vec{q}_1 \vec{b}_n}{2} + 1 \right] \cos 2\vec{q}_1 \left(\vec{r}_i + \frac{\vec{b}_n}{2} \right)}{\cos \vec{q}_1 \vec{b}_n - \cos 2\vec{q}_1 \left(\vec{r}_i + \frac{\vec{b}_n}{2} \right)}.$$

(B3)

The ϕ_n is a periodic, but bounded function.

For $B \to B$, the χ_n remains same. However, the $\phi_{ji}|_{i,j \in B} \to -\phi_{ji}|_{i,j \in A} + 2S\vec{q}_2\vec{b}_n$.[4] Explicitly,

$$\phi_{ji} = 2S\text{atan}\left[\frac{1}{\hbar(\vec{r}_i)\csc \vec{q}_2\vec{b}_n + \cot \vec{q}_2\vec{b}_n}\right] + 2S\vec{q}_2\vec{b}_n. \tag{B4}$$

For $A \to B$, the χ_{ji} is

$$e^{\chi_n} = w_n'^S\left[1 - g_n'\cos 2\vec{q}_1\left(\vec{r}_i + \frac{\vec{a}_n}{2}\right)\right]^S,$$

$$w_n' \equiv \frac{1}{2} - \left(\frac{1}{4} + \frac{\cos \vec{q}_2\vec{a}_n}{4}\right)\cos \vec{q}_1\vec{a}_n,$$

$$g_n' \equiv \left[\left(\frac{1}{4} - \frac{\cos \vec{q}_2\vec{a}_n}{4}\right)\Big/ w_n'\right], \tag{B5}$$

and the phase

$$e^{i\phi_{ji}} = e^{iS(\vec{q}_2\,\vec{a}_n - \pi)}. \tag{B6}$$

Substituting the above derived ϕ_n and χ_n in Eq. (A17) and assuming the interlattice hopping parameter (t_1) and intralattice hopping parameter (t_2), we find the total Hamiltonian:

$$H = -t_2 \sum_{i,j \in A} \bar{f}_i f_j w_n^S\left[1 + g_n\cos 2\vec{q}_1\left(\vec{r}_i + \frac{\vec{b}_n}{2}\right)\right]^S \exp\left\{+iS\left[2\text{atan}\left[\frac{1}{\hbar(\vec{r}_i)\csc \vec{q}_2\vec{b}_n + \cot \vec{q}_2\vec{b}_n}\right] - \vec{q}_2\vec{b}_n\right]\right\}$$

$$- t_2 \sum_{i,j \in B} \bar{f}_i f_j w_n^S\left[1 + g_n\cos 2\vec{q}_1\left(\vec{r}_i + \frac{\vec{b}_n}{2}\right)\right]^S \exp\left\{-iS\left[2\text{atan}\left[\frac{1}{\hbar(\vec{r}_i)\csc \vec{q}_2\vec{a}_n + \cot \vec{q}_2\vec{a}_n}\right] - \vec{q}_2\vec{a}_n\right]\right\}$$

$$+ t_1 \sum_{\substack{i \in A \\ j \in B}} \bar{f}_i f_j w_n'^S\left[1 - g_n'\cos 2\vec{q}_1\left(\vec{r}_i + \frac{\vec{a}_n}{2}\right)\right]^S. \tag{B7}$$

The first two terms—corresponding to the hopping either only on sublattice A, or on sublattice B respectively—are complex conjugate of each other. The third term corresponding to the hopping between sublattices A and B does not contain the imaginary part. Hence, the Hamiltonian and its complex conjugate are not identical to each other, which breaks the time reversal symmetry. At $\vec{q}_1 = (0,0)$ or at $\vec{q}_2 = (0,0)$, the ϕ_n in Eq. (B3) and (B4) collapses. In this case, there will not be any topological properties. It was expected as planar spin textures does not show any THE.

In momentum space, the two band Hamiltonian can be written as

$$H(\vec{k}) = \sum_{\vec{k}} \bar{\psi}_{\vec{k}} \mathcal{H}(\vec{k}) \psi_{\vec{k}}. \tag{B8}$$

The wave vector $\vec{k}$ is taken over the first Brillouin zone. The matrix $\psi_{\vec{k}} = [f_{k,A} f_{k,B}]$ contains the creation operators of the $\vec{k}$th momentum on the A and B sublattices. The single mode kernel of the Hamiltonian is $\mathcal{H}(\vec{k}) = \mathcal{H}_0(\vec{k}) \cdot \mathcal{I} + \mathcal{H}_i(\vec{k}) \cdot \vec{\sigma}_i$. Here, $\mathcal{I}$ is the unit matrix; $\vec{\sigma}_i$ are the Pauli matrices, and $\mathcal{H}_i(\vec{k})$ are the corresponding kernels.[5] To find an analytical formulation of $\mathcal{H}(\vec{k})$, we first represent

$$p(\vec{r}_i) \equiv \text{atan}\left[\frac{1}{\hbar(\vec{r}_i)\csc \vec{q}_2\vec{b}_n + \cot \vec{q}_2\vec{b}_n}\right]$$

$$= \sum_{k'} p(k')e^{-ik'r_i}, \tag{B9}$$

---

[4]On the B sublattice, $S_i \to -S_i$. Under this transformation, the ϕ_{ji} in Eq. (A14) can be written as

$$\phi_{ji}|_{i,j \in B} = iS\ln\frac{(S - S_i^z)(S - S_j^z) + S_i^- S_j^+}{(S - S_i^z)(S - S_j^z) + S_j^- S_i^+}$$

$$= iS\ln\frac{(S + S_i^z)(S + S_j^z) + S_j^- S_i^+}{(S + S_i^z)(S + S_j^z) + S_i^- S_j^+} \cdot \frac{S_j^+ S_i^-}{S_i^+ S_j^-}$$

$$= -\phi_{ji}|_{i,j \in A} + iS\ln e^{2i\vec{q}_2\vec{r}_j}e^{-2i\vec{q}_2\vec{r}_i}$$

$$= -\phi_{ji}|_{i,j \in A} + 2S\vec{q}_2\vec{b}_n.$$

[5]$\mathcal{H}(\vec{k})$ is a 2×2 matrix. In terms of the *Pauli matrices*, it is represented as

$$\mathcal{H}(\vec{k}) = \mathcal{H}_0\mathcal{I} + \mathcal{H}_x(\vec{k})\sigma_x + \mathcal{H}_y(\vec{k})\sigma_y + \mathcal{H}_z(\vec{k})\sigma_z,$$

where

$$\mathcal{H}_0(\vec{k}) = \frac{H_{i,j \in A} + H_{i,j \in B}}{2}, \mathcal{H}_x(\vec{k}) = \Re[H_{i \in A, j \in B}],$$

$$\mathcal{H}_z(\vec{k}) = \frac{H_{i,j \in A} - H_{i,j \in B}}{2}, \mathcal{H}_y(\vec{k}) = \Im[H_{i \in A, j \in B}].$$

Here, $\mathcal{I}$ is the 2×2 unit matrix; σ_x, σ_y, and σ_z are the Pauli matrices.

it is the Fourier series representation. As the value of $\mathcal{p}(k') \ll 1$ for most of the $\vec{q}_1, \vec{q}_2$ as shown in Figs. 3(c)–3(e), we can approximate

$$\exp\left\{i\,2S\text{atan}\left[\frac{1}{\hbar(\vec{r}_i)\csc\vec{q}_2\vec{b}_n + \cot\vec{q}_2\vec{b}_n}\right]\right\} \approx 1 + i2S\sum_{k'}\mathcal{p}(k')\mathrm{e}^{-ik'r}. \tag{B10}$$

Using above result the kernel $\mathcal{H}(\vec{k})$, can be written as

$$\mathcal{H}_0 = -2t_2 w_n^S \hat{\mathcal{F}}\left[1 + \mathcal{g}_n \cos 2q_1\left(\vec{r}_i + \frac{\vec{b}_n}{2}\right)\right]^S * \left\{\cos S\vec{q}_2\vec{b}_n \cos \vec{k}\vec{b}_n + 2S\sin S\vec{q}_2\vec{b}_n \sum_{k'}\mathcal{p}(k')\cos(\vec{k}+\vec{k}')\vec{b}_n\right\}$$

$$\mathcal{H}_x = +t_1 w_n'^S \hat{\mathcal{F}}\left[1 - \mathcal{g}_n' \cos 2q_1\left(\vec{r}_i + \frac{\vec{a}_n}{2}\right)\right]^S * \cos \vec{k}\vec{a}_n$$

$$\mathcal{H}_y = +t_1 w_n'^S \hat{\mathcal{F}}\left[1 - \mathcal{g}_n' \cos 2q_1\left(\vec{r}_i + \frac{\vec{a}_n}{2}\right)\right]^S * \sin \vec{k}\vec{a}_n$$

$$\mathcal{H}_z = -2t_2 w_n^S \hat{\mathcal{F}}\left[1 + \mathcal{g}_n \cos 2q_1\left(\vec{r}_i + \frac{\vec{b}_n}{2}\right)\right]^S * \left\{-\sin S\vec{q}_2\vec{b}_n \sin \vec{k}\vec{b}_n + 2S\cos S\vec{q}_2\vec{b}_n \sum_{k'}\mathcal{p}(k')\sin(\vec{k}+\vec{k}')\vec{b}_n\right\}. \tag{B11}$$

Here, $\hat{\mathcal{F}}$ represents the Fourier transform operator; $\langle\langle * \rangle\rangle$ is the convolution operator.

APPENDIX C: HAMILTONIAN FOR SPIN $S = 2, 3$

The Hamiltonian for $S = 2$ is found by first expanding the functions

$$\left[1 - \mathcal{g}_n' \cos 2\vec{q}_1\left(\vec{r}_i + \frac{\vec{a}_n}{2}\right)\right]^2, \left[1 + \mathcal{g}_n \cos 2\vec{q}_1\left(\vec{r}_i + \frac{\vec{b}_n}{2}\right)\right]^2 \tag{C1}$$

and then taking its Fourier transform. Substituting these Fourier transforms in Eq. (2) and taking the convolution, we will find the Hamiltonian:

$$\mathcal{H}_x = +t_1 \sum_n w_n'\left[\left(1 + \frac{\mathcal{g}_n'^2}{2}\right) - \mathcal{g}_n' \cos 2\vec{q}_1\vec{a}_n + \frac{\mathcal{g}_n'^2}{2}\cos 4\vec{q}_1\vec{a}_n\right]\cos \vec{k}\vec{a}_n,$$

$$\mathcal{H}_y = +t_1 \sum_n w_n'\left[\left(1 + \frac{\mathcal{g}_n'^2}{2}\right) - \mathcal{g}_n' \cos 2\vec{q}_1\vec{a}_n + \frac{\mathcal{g}_n'^2}{2}\cos 4\vec{q}_1\vec{a}_n\right]\sin \vec{k}\vec{a}_n,$$

$$\mathcal{H}_z = -2t_2 \sum_n w_n\left[\left(1 + \frac{\mathcal{g}_n^2}{2}\right) + \mathcal{g}_n \cos 2\vec{q}_1\vec{b}_n + \frac{\mathcal{g}_n^2}{2}\cos 4\vec{q}_1\vec{b}_n\right]\left\{-\sin 2\vec{q}_2\vec{b}_n \sin \vec{k}\vec{b}_n + 4\cos 2\vec{q}_2\vec{b}_n \sum_{\vec{k}'}\mathcal{p}(\vec{k}')\sin(\vec{k}+\vec{k}')\vec{b}_n\right\}. \tag{C2}$$

We dropped the $\mathcal{H}_0$ term as it does not play any role in determining the topological properties, besides it just adds an offset to overall energy. Comparing Eq. (C2) and Eq. (4), we see that they are analogous to each other. Hence, on a honeycomb lattice at $\pm\vec{K}$, the topological condition is satisfied, and the Chern number is defined by the $\vec{b}_1$ component of the $\mathcal{H}_z$.

In a similar way, we can find the Hamiltonian for $S = 3$. We take the cube of the terms containing $\mathcal{g}_n$ and $\mathcal{g}_n'$ in Eq. (2), and then take Fourier transform; the resulting Hamiltonian is

$$\mathcal{H}_x = +t_1 \sum_n w_n'\left[\left(1 + \frac{3\mathcal{g}_n'^2}{2}\right) - \left(3\mathcal{g}_n' + \frac{3\mathcal{g}_n'^3}{4}\right)\cos 2\vec{q}_1\vec{a}_n - \frac{3\mathcal{g}_n'^2}{2}\cos 4\vec{q}_1\vec{a}_n + \frac{\mathcal{g}_n'^3}{4}\cos 6\vec{q}_1\vec{a}_n\right]\cos \vec{k}\vec{a}_n,$$

$$\mathcal{H}_y = +t_1 \sum_n w_n'\left[\left(1 + \frac{3\mathcal{g}_n'^2}{2}\right) - \left(3\mathcal{g}_n' + \frac{3\mathcal{g}_n'^3}{4}\right)\cos 2\vec{q}_1\vec{a}_n - \frac{3\mathcal{g}_n'^2}{2}\cos 4\vec{q}_1\vec{a}_n + \frac{\mathcal{g}_n'^3}{4}\cos 6\vec{q}_1\vec{a}_n\right]\sin \vec{k}\vec{a}_n,$$

$$\mathcal{H}_z = -2t_2 \sum_n w_n\left[\left(1 + \frac{3\mathcal{g}_n^2}{2}\right) + \left(3\mathcal{g}_n + \frac{3\mathcal{g}_n^3}{4}\right)\cos 2\vec{q}_1\vec{b}_n - \frac{3\mathcal{g}_n^2}{2}\cos 4\vec{q}_1\vec{b}_n - \frac{\mathcal{g}_n^3}{4}\cos 6\vec{q}_1\vec{b}_n\right]$$

$$\times \left\{-\sin 3\vec{q}_2\vec{b}_n \sin \vec{k}\vec{b}_n + 6\cos 3\vec{q}_2\vec{b}_n \sum_{\vec{k}'}\mathcal{p}(\vec{k}')\sin(\vec{k}+\vec{k}')\vec{b}_n\right\}. \tag{C3}$$

We dropped the $\mathcal{H}_0$ term as it does not play any role in determining the topological properties, besides it just adds an offset to overall energy. Comparing Eq. (C3) and Eq. (4) we see that they are analogous to each other. Hence, on a honeycomb lattice at $\pm\vec{K}$ the topological condition is satisfied, and the Chern number is defined by the $\vec{b}_1$ component of the $\mathcal{H}_z$.

APPENDIX D: HAMILTONIAN FOR SPIN $S = 1/2$

Hamiltonian for $S = 1/2$ can be found only in limiting cases of $\mathcal{g}_n$ and $\mathcal{g}_n'$. Here, we find only for two cases (i) $\mathcal{g}_n' \ll 1$, $\mathcal{g}_n \ll 1$, (ii) $\mathcal{g}_n' \lessapprox 1$, $\mathcal{g}_n \ll 1$. When $\mathcal{g}_n \ll 1$, one can approximate:

$$
\left[1 + \mathcal{g}_n \cos 2\vec{q}_1\left(\vec{r}_i + \frac{\vec{b}_n}{2}\right)\right]^{1/2}
$$
$$
\approx \left[1 + \frac{\mathcal{g}_n}{2} \cos 2\vec{q}_1\left(\vec{r}_i + \frac{\vec{b}_n}{2}\right)\right]. \tag{D1}
$$

Similarly, for $\mathcal{g}_n' \ll 1$, one can approximate

$$
\left[1 - \mathcal{g}_n' \cos 2\vec{q}_1\left(\vec{r}_i + \frac{\vec{a}_n}{2}\right)\right]^{1/2}
$$
$$
\approx \left[1 - \frac{\mathcal{g}_n'}{2} \cos 2\vec{q}_1\left(\vec{r}_i + \frac{\vec{a}_n}{2}\right)\right]. \tag{D2}
$$

Taking Fourier transform of Eqs. (D1) and (D2) and substituting in Eq. (2), we will get the approximate Hamiltonian:

$$
\mathcal{H}_0 \approx -2t_2 \sum_n w_n \left[1 + \frac{\mathcal{g}_n}{4} \cos 2\vec{q}_1\vec{b}_n\right] \left\{ \cos \frac{\vec{q}_2\vec{b}_n}{2} \cos \vec{k}\vec{b}_n \right.
$$
$$
\left. + \sin \frac{\vec{q}_2\vec{b}_n}{2} \sum_{\vec{k}'} \mathcal{p}(\vec{k}') \cos(\vec{k} + \vec{k}')\vec{b}_n \right\},
$$
$$
\mathcal{H}_x \approx +t_1 \sum_n w_n' \left[1 - \frac{\mathcal{g}_n'}{4} \cos 2\vec{q}_1\vec{a}_n\right] \times \cos \vec{k}\vec{a}_n,
$$
$$
\mathcal{H}_y \approx +t_1 \sum_n w_n' \left[1 - \frac{\mathcal{g}_n'}{4} \cos 2\vec{q}_1\vec{a}_n\right] \times \sin \vec{k}\vec{a}_n,
$$
$$
\mathcal{H}_z \approx -2t_2 \sum_n w_n \left[1 + \frac{\mathcal{g}_n}{4} \cos 2\vec{q}_1\vec{b}_n\right] \left\{ -\sin \frac{\vec{q}_2\vec{b}_n}{2} \sin \vec{k}\vec{b}_n \right.
$$
$$
\left. + \cos \frac{\vec{q}_2\vec{b}_n}{2} \sum_{\vec{k}'} \mathcal{p}(\vec{k}') \sin(\vec{k} + \vec{k}')\vec{b}_n \right\}. \tag{D3}
$$

Comparing Eq. (D3) with Eq. (4), we see that they are analogous to each other. Hence, at $\pm K$ the $\mathcal{H}_x = \mathcal{H}_y = 0$, and the Chern number will be given only by the $\vec{b}_1$ component of the $\mathcal{H}_z$. Eq. (D3) is applicable in the regions shown in Fig. 5(a). The next case we consider is $\mathcal{g}_n' \lessapprox 1$, $\mathcal{g}_n \ll 1$. When $\mathcal{g}_n \gtrapprox 1$, we first make the change of variable $\mathcal{g}_n' = 1 - \gamma$; where γ
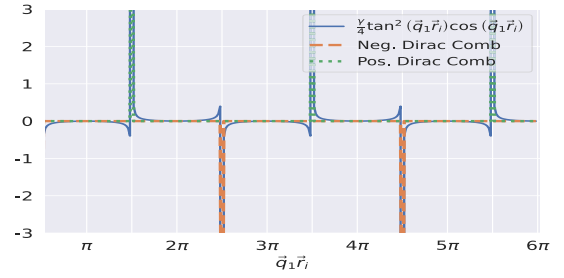

FIG. 11. Comparison of the term $\cos \vec{q}_1(\vec{r}_i + \frac{\vec{b}_n}{2})\frac{\gamma}{4} \tan^2 \vec{q}_1(\vec{r}_i + \frac{\vec{b}_n}{2})$ in Eq. (D4) with the Dirac comb (impulse train) with periodicity 2π. We took $\gamma = 0.1$ here. The whole function is summation of one positive and one negative Dirac comb shifted by π with respect to each other.

is a small quantity. It gives

$$
\left[1\,\mathcal{g}_n' \cos 2\vec{q}_1\left(\vec{r}_i + \frac{\vec{b}_n}{2}\right)\right]^{1/2}
$$
$$
\approx \sqrt{2} \cos \vec{q}_1\left(\vec{r}_i + \frac{\vec{b}_n}{2}\right)\left[\left(1 + \frac{\gamma}{4}\right) + \frac{\gamma}{4} \tan^2 \vec{q}_1\left(\vec{r}_i + \frac{\vec{b}_n}{2}\right)\right]. \tag{D4}
$$

Equation (D4) is applicable only when the condition $1 + \cos 2\vec{q}_1(\vec{r}_i - \frac{\vec{b}_n}{2}) \gg \gamma$ is satisfied. On the right-hand side of Eq. (D4), the term $\cos \vec{q}_1\vec{r}_i \frac{\gamma}{4} \tan^2 \vec{q}_1\vec{r}_i$ can be approximated as a combination of two Dirac comb ($\bot\!\!\!\bot$), one positive and other negative, as shown in Fig. 11. Hence we approximate

$$
\frac{\gamma}{4} \tan^2 \vec{q}_1\left(\vec{r}_i + \frac{\vec{b}_n}{2}\right) \cos \vec{q}_1\left(\vec{r}_i + \frac{\vec{b}_n}{2}\right)
$$
$$
\approx \bot\!\!\!\bot\left(\frac{3\pi}{2} + 2l\pi\right) - \bot\!\!\!\bot\left(\frac{\pi}{2} + 2l\pi\right);
$$
$$
\bot\!\!\!\bot\left(\frac{3\pi}{2} + 2l\pi\right)
$$
$$
\equiv \sum_{l\in\mathbb{Z}} \delta\left[\vec{q}_1\left(\vec{r}_i + \frac{\vec{b}_n}{2}\right) - \left(2l + \frac{3}{2}\right)\pi\right],
$$
$$
\bot\!\!\!\bot\left(\frac{\pi}{2} + 2l\pi\right)
$$
$$
\equiv \sum_{l\in\mathbb{Z}} \delta\left[\vec{q}_1\left(\vec{r}_i + \frac{\vec{b}_n}{2}\right) - \left(2l + \frac{1}{2}\right)\pi\right]. \tag{D5}
$$

Fourier transform of Dirac comb is a Dirac comb in the momentum space:

$$
\mathcal{F}\left[\bot\!\!\!\bot\left(\frac{3\pi}{2} + 2l\pi\right)\right] = \sum_{l\in\mathbb{Z}} \delta[\vec{k} - 2l\pi]. \tag{D6}
$$

Substituting Eq. (D4) with their approximate Dirac comb functions in Eq. (2) and taking Fourier transform, we

will find

$$\mathcal{H}_x \approx +\sqrt{2}t_1 \sum_n w'_n \left[\left(1 + \frac{\gamma}{4}\right) \cos \vec{q}_1 \vec{a}_n \right] \times \cos \vec{k} \vec{a}_n$$

$$\mathcal{H}_y \approx +\sqrt{2}t_1 \sum_n w'_n \left[\left(1 + \frac{\gamma}{4}\right) \cos \vec{q}_1 \vec{a}_n \right] \times \sin \vec{k} \vec{a}_n$$

$$\mathcal{H}_z \approx -2t_2 \sum_n w_n \left[1 + \frac{g_n}{4} \cos 2\vec{q}_1 \vec{b}_n\right] \left\{ -\sin \frac{\vec{q}_2 \vec{b}_n}{2} \sin \vec{k} \vec{b}_n + \cos \frac{\vec{q}_2 \vec{b}_n}{2} \sum_{\vec{k}'} \varphi(\vec{k}') \sin(\vec{k} + \vec{k}')\vec{b}_n \right\}. \tag{D7}$$

Comparing Eq. (D7) with Eq. (4), we see that they are analogous to each other. Hence, at $\pm\vec{K}$, the $\mathcal{H}_x = \mathcal{H}_y = 0$, and the Chern number will be given only by the $\vec{b}_1$ component of the $\mathcal{H}_z$. Equation (D3) is applicable in the regions shown in Fig. 5(a).

APPENDIX E: HAMILTONIAN FOR $S = 3/2$

As in $S = 1/2$, the Hamiltonian for $S = 3/2$ is found in the limiting cases of g_n and g'_n. As in Sec. D here also we consider only two cases (i) $g'_n \ll 1$, $g_n \ll 1$ and (ii) $g'_n \lesssim 1$, $g_n \ll 1$. The idea is to represent the terms containing g_n with half-integer powers as the multiplication of the integer power and square root, i.e., for $S = 3/2$,

$$\left[1 + g_n \cos 2\vec{q}_1 \left(\vec{r}_i + \frac{\vec{b}_n}{2}\right)\right]^{3/2} = \left[1 + g_n \cos 2\vec{q}_1 \left(\vec{r}_i + \frac{\vec{b}_n}{2}\right)\right] \left[1 + \frac{g_n}{2} \cos 2\vec{q}_1 \left(\vec{r}_i + \frac{\vec{b}_n}{2}\right)\right]^{1/2}. \tag{E1}$$

Then we can apply the approximation of limiting cases to the square root term as described in Sec. D. It should be kept in mind that, after this step the resulting equations are applicable only to the limiting values of q_{1x} and q_{2x}; for the case of honeycomb lattice, it is shown in Fig. 5(a). Further we take Fourier transform of the resulting terms to find the full Hamiltonian. Following this procedure for $S = 3/2$ and for the case $g_n \ll 1$ and $g'_n \ll 1$, we find

$$\mathcal{H}_x \approx +t_1 \sum_n w'_n \left[\left(1 + \frac{g'^2_n}{4}\right) - \frac{3}{2} g'_n \cos 2\vec{q}_1 \vec{a}_n + \frac{g'^2_n}{4} \cos 4\vec{q}_1 \vec{a}_n \right] \cos \vec{k} \vec{a}_n,$$

$$\mathcal{H}_y \approx +t_1 \sum_n w'_n \left[\left(1 + \frac{g'^2_n}{4}\right) - \frac{3}{2} g'_n \cos 2\vec{q}_1 \vec{a}_n + \frac{g'^2_n}{4} \cos 4\vec{q}_1 \vec{a}_n \right] \sin \vec{k} \vec{a}_n,$$

$$\mathcal{H}_z \approx -2t_2 \sum_n w_n \left[\left(1 + \frac{g^2_n}{4}\right) + \frac{3}{2} g_n \cos 2\vec{q}_1 \vec{b}_n + \frac{g^2_n}{4} \cos 4\vec{q}_1 \vec{b}_n \right] \left\{ -\sin \frac{\vec{q}_2 \vec{b}_n}{2} \sin \vec{k} \vec{b}_n + \cos \frac{\vec{q}_2 \vec{b}_n}{2} \sum_{\vec{k}'} \varphi(\vec{k}') \sin(\vec{k} + \vec{k}')\vec{b}_n \right\}. \tag{E2}$$

Comparing Eq. (E2) and Eq. (4), we see that they are analogous to each other. Hence, for the honeycomb lattice the topological condition is satisfied at $\pm\vec{K}$. Besides, the Chern number is given by the $\vec{b}_1$ component of $\mathcal{H}_z$.

For $g_n \ll 1$ and $g'_n \lesssim 1$ the Hamiltonian is

$$\mathcal{H}_x \approx +\sqrt{2}t_1 \sum_n w'_n \left[\left(\frac{3}{4} + \frac{g'_n}{4}\right) \left(\cos 2\vec{q}_1 \vec{a}_n + g'_n \cos 4\vec{q}_1 \vec{a}_n\right) \right] \cos \vec{k} \vec{a}_n,$$

$$\mathcal{H}_y \approx +\sqrt{2}t_1 \sum_n w'_n \left[\left(\frac{3}{4} + \frac{g'_n}{4}\right) \left(\cos 2\vec{q}_1 \vec{a}_n + g'_n \cos 4\vec{q}_1 \vec{a}_n\right) \right] \sin \vec{k} \vec{a}_n,$$

$$\mathcal{H}_z \approx -2t_2 \sum_n w_n \left[\left(1 + \frac{g^2_n}{4}\right) + \frac{3}{2} g_n \cos 2\vec{q}_1 \vec{b}_n + \frac{g^2_n}{4} \cos 4\vec{q}_1 \vec{b}_n \right] \left\{ -\sin \frac{\vec{q}_2 \vec{b}_n}{2} \sin \vec{k} \vec{b}_n + \cos \frac{\vec{q}_2 \vec{b}_n}{2} \sum_{\vec{k}'} \varphi(\vec{k}') \sin(\vec{k} + \vec{k}')\vec{b}_n \right\}. \tag{E3}$$

Here also Eq. (E3) is analogous to Eq. (4). Hence, the Chern number is given by $\vec{b}_1$ component of $\mathcal{H}_z$ on a honeycomb lattice.

APPENDIX F: CHERN NUMBER CALCULATIONS FOR HONEYCOMB BIPARTITE LATTICE

We calculate the Chern number (c_1) for $S = 1$ using the Hamiltonian Eq. (4). c_1 is calculated at momentum $\pm \vec{K}$ when the condition $\mathcal{H}_x = \mathcal{H}_y = 0$ and $\mathcal{H}_z \neq 0$ is satisfied simultaneously (see Sec. 3.5.6 of Ref. [55]). If we take $\vec{q}_1 = (2q_{1x}/\sqrt{3}, 0)$ and $\vec{q}_2 = (2q_{2x}/\sqrt{3}, 0)$, then at the point $\pm \vec{K} = (\pm \pi /\sqrt{3}, 0)$ the condition is satisfied identically. To see this, first we introduce the three NN (a_n) and NNN (b_n) lattice vectors of the honeycomb lattice, and expand Eq. (4):

$$\mathcal{H}_x = + t_1 w'_1 \left[1 - \frac{g'_1}{2} \cos 2\vec{q}_1\vec{a}_1\right] \times \cos \vec{k}\vec{a}_1 + t_1 w'_2 \left[1 - \frac{g'_2}{2} \cos 2\vec{q}_1\vec{a}_2\right] \times \cos \vec{k}\vec{a}_2 + t_1 w'_3 \left[1 - \frac{g'_3}{2} \cos 2\vec{q}_1\vec{a}_3\right] \times \cos \vec{k}\vec{a}_3,$$
(F1)

$$\mathcal{H}_y = + t_1 w'_1 \left[1 - \frac{g'_1}{2} \cos 2\vec{q}_1\vec{a}_1\right] \times \sin \vec{k}\vec{a}_1 + t_1 w'_2 \left[1 - \frac{g'_2}{2} \cos 2\vec{q}_1\vec{a}_2\right] \times \sin \vec{k}\vec{a}_2 + t_1 w'_3 \left[1 - \frac{g'_3}{2} \cos 2\vec{q}_1\vec{a}_3\right] \times \sin \vec{k}\vec{a}_3,$$
(F2)

$$\mathcal{H}_z = -2t_2 w_1 \left[1 + \frac{g_1}{2} \cos 2\vec{q}_1\vec{b}_1\right] \left\{-\sin \vec{q}_2\vec{b}_1 \sin \vec{k}\vec{b}_1 + 2\cos \vec{q}_2\vec{b}_1 \sum_{k'} p(k') \sin(\vec{k} + \vec{k}')\vec{b}_1\right\} - 2t_2 w_2 \left[1 + \frac{g_2}{2} \cos 2\vec{q}_1\vec{b}_2\right]$$

$$\times \left\{-\sin \vec{q}_2\vec{b}_2 \sin \vec{k}\vec{b}_2 + 2\cos \vec{q}_2\vec{b}_2 \sum_{k'} p(k') \sin(\vec{k} + \vec{k}')\vec{b}_2\right\} - 2t_2 w_3 \left[1 + \frac{g_3}{2} \cos 2\vec{q}_1\vec{b}_3\right]$$

$$\times \left\{-\sin \vec{q}_2\vec{b}_3 \sin \vec{k}\vec{b}_3 + 2\cos \vec{q}_2\vec{b}_3 \sum_{k'} p(k') \sin(\vec{k} + \vec{k}')\vec{b}_3\right\}.$$
(F3)

In Eqs. (F1)–(F3), we explicitly wrote all the three components of the $\mathcal{H}_x$, $\mathcal{H}_y$ and H_z, respectively We dropped the $\mathcal{H}_0$ component as it does not play any role in determining the c_1. Further one need to substitute the values of $\vec{a}_n$, $\vec{b}_n$, $\vec{q}_1 = (2q_{1x}/\sqrt{3}, 0)$, $\vec{q}_2 = (2q_{2x}/\sqrt{3}, 0)$, and $\pm \vec{K} = (\pm \pi /\sqrt{3}, 0)$ in above equations. In Table II, we have given the dot product of these values. Substituting these in Eqs. (F1)–(F3), we will get

$$\mathcal{H}_x = 0,$$
(F4)

$$\mathcal{H}_y = \pm t_1 w'_1 \left[1 - \frac{g'_1}{2} \cos 2\vec{q}_{1x}\right] \mp t_1 w'_2 \left[1 - \frac{g'_2}{2} \cos 2\vec{q}_{1x}\right] = 0,$$
(F5)

$$\mathcal{H}_z = -2t_2 w_1 \left[1 + \frac{g_1}{2} \cos 2q_{1x}\right] \left\{\pm \sin \vec{q}_{2x} + 2\cos q_{2x} \sum_{k'} p(k') \sin(\pm \pi /2 + \vec{k}'\vec{b}_1)\right\} - 2t_2 w_2 \left[1 + \frac{g_2}{2} \cos 2q_{1x}\right]$$

$$\times \left\{\pm \sin \vec{q}_{2x} + 2\cos q_{2x} \sum_{k'} p(k') \sin(\pm \pi /2 + \vec{k}'\vec{b}_2)\right\} - 2t_2 w_3 \left[1 + \frac{g_3}{2} \cos 2q_{1x}\right] \left\{+2\cos q_{2x} \sum_{k'} p(k') \sin(\pm \pi + \vec{k}'\vec{b}_3)\right\}.$$
(F6)

We observe that all the terms of $\mathcal{H}_x$ are identically zero; the term involving $\vec{a}_1$ and $\vec{a}_2$ are zero as $\cos \vec{k}\vec{a}_1 = \cos \pi /2 = 0$ and $\cos \vec{k}\vec{a}_2 = \cos \pi /2 = 0$; the term involving a_3 is zero as $w_3 = 0$. For $\mathcal{H}_y$, the summation of all three terms are zero;

TABLE II. Table showing dot product between NN ($\vec{a}_n$) and NNN ($\vec{b}_n$) lattice vectors of the honeycomb lattice and vectors $\vec{q}_1$, $\vec{q}_2$, $\pm \vec{K}$.

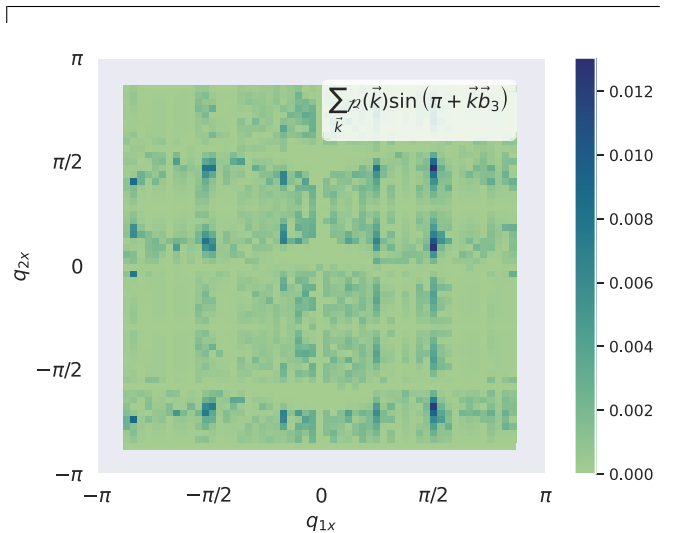| Lat. Vect.	$\vec{q}_1 = (\frac{2q_{1x}}{\sqrt{3}}, 0)$	$\vec{q}_2 = (\frac{2q_{2x}}{\sqrt{3}}, 0)$	$\pm \vec{K} = (\pm \frac{\pi}{\sqrt{3}}, 0)$
$\vec{a}_1 = (\frac{\sqrt{3}}{2}, \frac{1}{2})$	q_{1x}	q_{2x}	$\pm \frac{\pi}{2}$
$\vec{a}_2 = (\frac{-\sqrt{3}}{2}, \frac{1}{2})$	$-q_{1x}$	$-q_{2x}$	$\mp \frac{\pi}{2}$
$\vec{a}_3 = (0, 1)$	0	0	0
$\vec{b}_1 = (\frac{-\sqrt{3}}{2}, \frac{3}{2})$	$-q_{1x}$	$-q_{2x}$	$\mp \frac{\pi}{2}$
$\vec{b}_2 = (\frac{-\sqrt{3}}{2}, \frac{3}{2})$	$-q_{1x}$	$-q_{2x}$	$\mp \frac{\pi}{2}$
$\vec{b}_3 = (\sqrt{3}, 0)$	$2q_{1x}$	$2q_{2x}$	$\pm \pi$

FIG. 12. Dependence of $\sum_{k'} p(k') \sin(\pi + k'b_3)$ on $\vec{q}_1 = (q_{1x}, 0)$ and $\vec{q}_2 = (q_{2x}, 0)$. In the figure, only the q_{1x} and q_{2x} value changes from $-\sqrt{3}\pi /2$ to $\sqrt{3}\pi /2$.

the term involving $\vec{a}_3$ is zero as $\sin \vec{k}a_3 = \sin 0 = 0$; the terms involving $\vec{a}_1$ and $\vec{a}_2$ are opposite of each other, hence they cancel. The three terms of the $\mathcal{H}_z$ are not zero at $\pm \vec{K}$. For $\mathcal{H}_z$, in the term containing $\vec{b}_3$, one can observe that both $\wp(k') \sim 0$ (see Fig. 12) and the term $\sin(\pm\pi + \vec{k}'\vec{b}_3) \sim 0$; hence, we can neglect this term due to at least an order of smallness compared to other two terms (containing $\vec{b}_1$ and $\vec{b}_2$). The values

of $\mathscr{q}'_n$ and $\mathscr{w}_n$ are always positive and less than unity. Hence, they also will not have any effect on Chern number. The terms containing $\vec{b}_1$ and $\vec{b}_2$ controls the Chern number. The first Chern number is calculated by using Eq. (5). Observing the Hamiltonian of Eqs. (B11), (C2), (C3), (D3), (D7), (E2), and (E3), we see that the property where c_1 depends only on $\vec{b}_1$ (or b_2) is also applicable.

---

[1] P. Bruno, V. K. Dugaev, and M. Taillefumier, Topological Hall effect and Berry phase in magnetic nanostructures, Phys. Rev. Lett. **93**, 096806 (2004).

[2] S.-S. Zhang, H. Ishizuka, H. Zhang, G. B. Halász, and C. D. Batista, Real-space Berry curvature of itinerant electron systems with spin-orbit interaction, Phys. Rev. B **101**, 024420 (2020).

[3] H. Wang, Y. Dai, G.-M. Chow, and J. Chen, Topological hall transport: Materials, mechanisms and potential applications, Prog. Mater. Sci. **130**, 100971 (2022).

[4] R. Wiesendanger, Nanoscale magnetic skyrmions in metallic films and multilayers: A new twist for spintronics, Nat. Rev. Mater. **1**, 16044 (2016).

[5] A. Fert, N. Reyren, and V. Cros, Magnetic skyrmions: Advances in physics and potential applications, Nat. Rev. Mater. **2**, 17031 (2017).

[6] M. Ezawa, Giant skyrmions stabilized by dipole-dipole interactions in thin ferromagnetic films, Phys. Rev. Lett. **105**, 197202 (2010).

[7] C. D. Batista, S.-Z. Lin, S. Hayami, and Y. Kamiya, Frustration and chiral orderings in correlated electron systems, Rep. Prog. Phys. **79**, 084504 (2016).

[8] K. Karube, J. S. White, D. Morikawa, C. D. Dewhurst, R. Cubitt, A. Kikkawa, X. Yu, Y. Tokunaga, T.-h. Arima, H. M. Rønnow, Y. Tokura, and Y. Taguchi, Disordered skyrmion phase stabilized by magnetic frustration in a chiral magnet, Sci. Adv. **4**, eaar7043 (2018).

[9] A. O. Leonov, I. M. Tambovtcev, I. S. Lobanov, and V. M. Uzdin, Stability of in-plane and out-of-plane chiral skyrmions in epitaxial MnSi(111)/Si(111) thin films: Surface twists versus easy-plane anisotropy, Phys. Rev. B **102**, 174415 (2020).

[10] M. Preißinger, K. Karube, D. Ehlers, B. Szigeti, H.-A. Krug von Nidda, J. S. White, V. Ukleev, H. M. Rønnow, Y. Tokunaga, A. Kikkawa, Y. Tokura, Y. Taguchi, and I. Kézsmárki, Vital role of magnetocrystalline anisotropy in cubic chiral skyrmion hosts, npj Quantum Mater. **6**, 1 (2021).

[11] R. Ozawa, S. Hayami, and Y. Motome, Zero-field skyrmions with a high topological number in itinerant magnets, Phys. Rev. Lett. **118**, 147205 (2017).

[12] H. Komatsu, Y. Nonomura, and M. Nishino, Phase diagram of the two-dimensional dipolar Heisenberg model with Dzyaloshinskii-Moriya interaction and Ising anisotropy, Phys. Rev. B **103**, 214404 (2021).

[13] B. Li, J.-Q. Yan, D. M. Pajerowski, E. Gordon, A.-M. Nedić, Y. Sizyuk, L. Ke, P. P. Orth, D. Vaknin, and R. J. McQueeney, Competing magnetic interactions in the antiferromagnetic topological insulator $MnBi_2Te_4$, Phys. Rev. Lett. **124**, 167204 (2020).

[14] W. Sun, W. Wang, J. Zang, H. Li, G. Zhang, J. Wang, and Z. Cheng, Manipulation of magnetic skyrmion in a 2D van der Waals heterostructure via both electric and magnetic fields, Adv. Funct. Mater. **31**, 2104452 (2021).

[15] A. Bernand-Mantel, C. B. Muratov, and T. M. Simon, Unraveling the role of dipolar versus Dzyaloshinskii-Moriya interactions in stabilizing compact magnetic skyrmions, Phys. Rev. B **101**, 045416 (2020).

[16] J. F. Sierra, J. Fabian, R. K. Kawakami, S. Roche, and S. O. Valenzuela, Van der Waals heterostructures for spintronics and opto-spintronics, Nat. Nanotechnol. **16**, 856 (2021).

[17] K. S. Burch, D. Mandrus, and J.-G. Park, Magnetism in two-dimensional van der Waals materials, Nature (London) **563**, 47 (2018).

[18] S. Yang, T. Zhang, and C. Jiang, Van der Waals magnets: Material family, detection and modulation of magnetism, and perspective in spintronics, Adv. Sci. **8**, 2002488 (2021).

[19] Q. Tong, M. Chen, and W. Yao, Magnetic proximity effect in a van der Waals Moire superlattice, Phys. Rev. Appl. **12**, 024031 (2019).

[20] P. Jiang, C. Wang, D. Chen, Z. Zhong, Z. Yuan, Z.-Y. Lu, and W. Ji, Stacking tunable interlayer magnetism in bilayer CrI_3, Phys. Rev. B **99**, 144401 (2019).

[21] S. K. Behura, A. Miranda, S. Nayak, K. Johnson, P. Das, and N. R. Pradhan, Moiré physics in twisted van der Waals heterostructures of 2D materials, Emergent Mater. **4**, 813 (2021).

[22] K. Tran, J. Choi, and A. Singh, Moiré and beyond in transition metal dichalcogenide twisted bilayers, 2D Mater. **8**, 022002 (2021).

[23] K. F. Mak, J. Shan, and D. C. Ralph, Probing and controlling magnetic states in 2D layered magnetic materials, Nat. Rev. Phys. **1**, 646 (2019).

[24] Q. H. Wang, A. Bedoya-Pinto, M. Blei, A. H. Dismukes, A. Hamo, S. Jenkins, M. Koperski, Y. Liu, Q.-C. Sun, E. J. Telford, H. H. Kim, M. Augustin, U. Vool, J.-X. Yin, L. H. Li, A. Falin, C. R. Dean, F. Casanova, R. F. L. Evans, M. Chshiev *et al.*, The magnetic genome of two-dimensional van der Waals materials, ACS Nano **16**, 6960 (2022).

[25] H. Kurebayashi, J. H. Garcia, S. Khan, J. Sinova, and S. Roche, Magnetism, symmetry and spin transport in van der Waals layered systems, Nat. Rev. Phys. **4**, 150 (2022).

[26] Y. Zhang, Y. Gu, H. Weng, K. Jiang, and J. Hu, Mottness in two-dimensional van der Waals Nb_3X_8 monolayers (X=Cl, Br and I), Phys. Rev. B **107**, 035126 (2023).

[27] M. Corasaniti, R. Yang, K. Sen, K. Willa, M. Merz, A. A. Haghighirad, M. Le Tacon, and L. Degiorgi, Electronic correlations in the van der Waals ferromagnet Fe_3GeTe_2 revealed by its charge dynamics, Phys. Rev. B **102**, 161109 (2020).

[28] S. Sarkar and P. Kratzer, Electronic correlation, magnetic structure, and magnetotransport in few-layer CrI_3, Phys. Rev. Mater. **4**, 104006 (2020).

[29] J.-X. Zhu, M. Janoschek, D. S. Chaves, J. C. Cezar, T. Durakiewicz, F. Ronning, Y. Sassa, M. Mansson, B. L. Scott, N. Wakeham, E. D. Bauer, and J. D. Thompson, Electronic correlation and magnetism in the ferromagnetic metal Fe_3GeTe_2, Phys. Rev. B **93**, 144404 (2016).

[30] S. Ghosh, S. Ershadrad, V. Borisov, and B. Sanyal, Unraveling effects of electron correlation in two-dimensional Fe_nGeTe_2 ($n = 3, 4, 5$) by dynamical mean field theory, npj Comput. Mater. **9**, 86 (2023).

[31] K. K. Kesharpu, E. A. Kochetov, and A. Ferraz, Topological Hall effect induced by classical large-spin background: su(2) path-integral approach, Phys. Rev. B **107**, 155146 (2023).

[32] M. J. Meijer, J. Lucassen, R. A. Duine, H. J. Swagten, B. Koopmans, R. Lavrijsen, and M. H. D. Guimarães, Chiral spin spirals at the surface of the van der Waals ferromagnet Fe_3GeTe_2, Nano Lett. **20**, 8563 (2020).

[33] M.-G. Han, J. A. Garlow, Y. Liu, H. Zhang, J. Li, D. DiMarzio, M. W. Knight, C. Petrovic, D. Jariwala, and Y. Zhu, Topological magnetic-spin textures in two-dimensional van der Waals $Cr_2Ge_2Te_6$, Nano Lett. **19**, 7859 (2019).

[34] Z. Fei, B. Huang, P. Malinowski, W. Wang, T. Song, J. Sanchez, W. Yao, D. Xiao, X. Zhu, A. F. May, W. Wu, D. H. Cobden, J.-H. Chu, and X. Xu, Two-dimensional itinerant ferromagnetism in atomically thin Fe_3GeTe_2, Nat. Mater. **17**, 778 (2018).

[35] Y. Zhang, H. Lu, X. Zhu, S. Tan, W. Feng, Q. Liu, W. Zhang, Q. Chen, Y. Liu, X. Luo, D. Xie, L. Luo, Z. Zhang, and X. Lai, Emergence of Kondo lattice behavior in a van der Waals itinerant ferromagnet, Fe_3GeTe_2, Sci. Adv. **4**, eaao6791 (2018).

[36] B. Ding, X. Li, Z. Li, X. Xi, Y. Yao, and W. Wang, Tuning the density of zero-field skyrmions and imaging the spin configuration in a two-dimensional Fe_3GeTe_2 magnet, NPG Asia Materials **14**, 74 (2022).

[37] L. Peng, F. S. Yasin, T.-E. Park, S. J. Kim, X. Zhang, T. Nagai, K. Kimoto, S. Woo, and X. Yu, Tunable Néel–Bloch magnetic twists in Fe_3GeTe_2 with van der Waals structure, Adv. Funct. Mater. **31**, 2103583 (2021).

[38] Y. Gao, S. Yan, Q. Yin, H. Huang, Z. Li, Z. Zhu, J. Cai, B. Shen, H. Lei, Y. Zhang, and S. Wang, Manipulation of topological spin configuration via tailoring thickness in van der Waals ferromagnetic $Fe_{5-x}GeTe_2$, Phys. Rev. B **105**, 014426 (2022).

[39] I. Lemesh and G. S. D. Beach, Twisted domain walls and skyrmions in perpendicularly magnetized multilayers, Phys. Rev. B **98**, 104402 (2018).

[40] G. Chen, T. Ma, A. T. N'Diaye, H. Kwon, C. Won, Y. Wu, and A. K. Schmid, Tailoring the chirality of magnetic domain walls by interface engineering, Nat. Commun. **4**, 2671 (2013).

[41] J. A. Garlow, S. D. Pollard, M. Beleggia, T. Dutta, H. Yang, and Y. Zhu, Quantification of mixed Bloch-N'eel topological spin textures stabilized by the dzyaloshinskii-moriya interaction in Co/Pd multilayers, Phys. Rev. Lett. **122**, 237201 (2019).

[42] G. Chen, J. Zhu, A. Quesada, J. Li, A. T. N'Diaye, Y. Huo, T. P. Ma, Y. Chen, H. Y. Kwon, C. Won, Z. Q. Qiu, A. K. Schmid, and Y. Z. Wu, Novel chiral magnetic domain Wall structure in Fe/Ni/Cu(001) films, Phys. Rev. Lett. **110**, 177204 (2013).

[43] E. C. S. F. R. S, Ferromagnetism, Rep. Prog. Phys. **11**, 43 (1947).

[44] I. Ivantsov, A. Ferraz, and E. Kochetov, Strong correlation, Bloch bundle topology, and spinless Haldane–Hubbard model, Ann. Phys. **441**, 168859 (2022).

[45] A. Ferraz and E. Kochetov, Fractionalization of strongly correlated electrons as a possible route to quantum Hall effect without magnetic field, Phys. Rev. B **105**, 245128 (2022).

[46] A. Ferraz and E. A. Kochetov, Effective action for strongly correlated electron systems, Nucl. Phys. B **853**, 710 (2011).

[47] F. A. Berezin, in *Introduction to Superanalysis*, edited by A. A. Kirillov (Springer Netherlands, Dordrecht, 1987).

[48] M. Lavagna and C. Pepin, The kondo lattice model, Acta Phys. Pol. B **29**, 3753 (1998).

[49] H. Tsunetsugu, M. Sigrist, and K. Ueda, The ground-state phase diagram of the one-dimensional Kondo lattice model, Rev. Mod. Phys. **69**, 809 (1997).

[50] P. Coleman, *Introduction to Many-Body Physics*, 1st ed. (Cambridge University Press, Cambridge, 2015).

[51] P. Aynajian, E. H. da Silva Neto, A. Gyenis, R. E. Baumbach, J. D. Thompson, Z. Fisk, E. D. Bauer, and A. Yazdani, Visualizing heavy fermions emerging in a quantum critical Kondo lattice, Nature (London) **486**, 201 (2012).

[52] M. Shimozawa, S. K. Goh, T. Shibauchi, and Y. Matsuda, From Kondo lattices to Kondo superlattices, Rep. Prog. Phys. **79**, 074503 (2016).

[53] X. Wu, L. Lei, Q. Yin, N.-N. Zhao, M. Li, Z. Wang, Q. Liu, W. Song, H. Ma, P. Ding, Z. Cheng, K. Liu, H. Lei, and S. Wang, Direct observation of competition between charge order and itinerant ferromagnetism in the van der Waals crystal $Fe_{5-x}GeTe_2$, Phys. Rev. B **104**, 165101 (2021).

[54] V. Vaňo, M. Amini, S. C. Ganguli, G. Chen, J. L. Lado, S. Kezilebieke, and P. Liljeroth, Artificial heavy fermions in a van der Waals heterostructure, Nature (London) **599**, 582 (2021).

[55] M. Fruchart and D. Carpentier, An introduction to topological insulators, C. R. Phys. **14**, 779 (2013).

[56] N. Nagaosa and Y. Tokura, Topological properties and dynamics of magnetic skyrmions, Nat. Nanotechnol. **8**, 899 (2013).

[57] F. D. M. Haldane, Model for a quantum hall effect without landau levels: Condensed-matter realization of the "parity anomaly", Phys. Rev. Lett. **61**, 2015 (1988).

[58] M. Joe, P. K. Srivastava, B. Singh, H. Ahn, and C. Lee, Iron-based ferromagnetic van der Waals materials, J. Phys. D **54**, 473002 (2021).

[59] J. Seo, D. Y. Kim, E. S. An, K. Kim, G.-Y. Kim, S.-Y. Hwang, D. W. Kim, B. G. Jang, H. Kim, G. Eom, S. Y. Seo, R. Stania, M. Muntwiler, J. Lee, K. Watanabe, T. Taniguchi, Y. J. Jo, J. Lee, B. I. Min, M. H. Jo *et al.*, Nearly room temperature ferromagnetism in a magnetic metal-rich van der Waals metal, Sci. Adv. **6**, eaay8912 (2020).

[60] D. Kim, C. Lee, B. G. Jang, K. Kim, and J. H. Shim, Drastic change of magnetic anisotropy in Fe_3GeTe_2 and Fe_4GeTe_2 monolayers under electric field studied by density functional theory, Sci. Rep. **11**, 17567 (2021).

[61] D. Rana, M. Bhakar, B. G., S. Bera, N. Saini, S. K. Pradhan, M. Mondal, M. Kabir, and G. Sheet, High transport spin polarization in the van der Waals ferromagnet Fe_4GeTe_2, Phys. Rev. B **107**, 224422 (2023).

[62] K. Yamagami, Y. Fujisawa, B. Driesen, C. H. Hsu, K. Kawaguchi, H. Tanaka, T. Kondo, Y. Zhang, H. Wadati, K. Araki, T. Takeda, Y. Takeda, T. Muro, F. C. Chuang, Y. Niimi, K. Kuroda, M. Kobayashi, and Y. Okada, Itinerant ferromagnetism mediated by giant spin polarization of the metallic ligand band in the van der Waals magnet Fe_5GeTe_2, Phys. Rev. B **103**, L060403 (2021).

[63] X. Xu, Y. W. Li, S. R. Duan, S. L. Zhang, Y. J. Chen, L. Kang, A. J. Liang, C. Chen, W. Xia, Y. Xu, P. Malinowski, X. D. Xu, J.-H. Chu, G. Li, Y. F. Guo, Z. K. Liu, L. X. Yang, and Y. L. Chen, Signature for non-Stoner ferromagnetism in the van der Waals ferromagnet Fe_3GeTe_2, Phys. Rev. B **101**, 201104(R) (2020).

[64] H. Wang, H. Lu, Z. Guo, A. Li, P. Wu, J. Li, W. Xie, Z. Sun, P. Li, H. Damas, A. M. Friedel, S. Migot, J. Ghanbaja, L. Moreau, Y. Fagot-Revurat, S. Petit-Watelot, T. Hauet, J. Robertson, S. Mangin, W. Zhao *et al.*, Interfacial engineering of ferromagnetism in wafer-scale van der Waals Fe_4GeTe_2 far above room temperature, Nat. Commun. **14**, 2483 (2023).

[65] M. Gulacsi, The Kondo lattice model, Philos. Mag. **86**, 1907 (2006).

[66] G. Kimbell, C. Kim, W. Wu, M. Cuoco, and J. W. A. Robinson, Challenges in identifying chiral spin textures via the topological Hall effect, Commun. Mater **3**, 19 (2022).

[67] Y. Li, R. Basnet, K. Pandey, J. Hu, W. Wang, X. Ma, A. R. C. McCray, A. K. Petford-Long, and C. Phatak, Field-Dependent magnetic domain behavior in van der Waals Fe_3GeTe_2, JOM **74**, 2310 (2022).

[68] T.-E. Park, L. Peng, J. Liang, A. Hallal, F. S. Yasin, X. Zhang, K. M. Song, S. J. Kim, K. Kim, M. Weigand, G. Schütz, S. Finizio, J. Raabe, K. Garcia, J. Xia, Y. Zhou, M. Ezawa, X. Liu, J. Chang, H. C. Koo *et al.*, N'eel-type skyrmions and their current-induced motion in van der Waals ferromagnet-based heterostructures, Phys. Rev. B **103**, 104410 (2021).

[69] C. Liu, J. Jiang, C. Zhang, Q. Wang, H. Zhang, D. Zheng, Y. Li, Y. Ma, H. Algaidi, X. Gao, Z. Hou, W. Mi, J.-M. Liu, Z. Qiu, and X. Zhang, Controllable skyrmionic phase transition between Néel skyrmions and Bloch skyrmionic bubbles in van der Waals ferromagnet $Fe_{3-\delta}GeTe_2$, Adv. Sci. (Weinheim, Baden-Wurttemberg, Germany) **10**, e2303443 (2023).

[70] Z. Li, H. Zhang, G. Li, J. Guo, Q. Wang, Y. Deng, Y. Hu, X. Hu, C. Liu, M. Qin, X. Shen, R. Yu, X. Gao, Z. Liao, J. Liu, Z. Hou, Y. Zhu, and X. Fu, Room-temperature sub-100 nm Néel-type skyrmions in non-stoichiometric van der Waals ferromagnet $Fe_{3-x}GaTe_2$ with ultrafast laser writability, Nat. Commun. **15**, 1017 (2024).

[71] X. Yao, D. Hu, and S. Dong, Modulation of skyrmionic magnetic textures in two-dimensional vdW materials and their heterostructures, iScience **26**, 106311 (2023).

[72] Y. Wu, S. Zhang, J. Zhang, W. Wang, Y. L. Zhu, J. Hu, G. Yin, K. Wong, C. Fang, C. Wan, X. Han, Q. Shao, T. Taniguchi, K. Watanabe, J. Zang, Z. Mao, X. Zhang, and K. L. Wang, Néel-type skyrmion in WTe_2/Fe_3GeTe_2 van der Waals heterostructure, Nat. Commun. **11**, 3860 (2020).

[73] M. Yang, Q. Li, R. V. Chopdekar, R. Dhall, J. Turner, J. D. Carlström, C. Ophus, C. Klewe, P. Shafer, A. T. N'Diaye,

J. W. Choi, G. Chen, Y. Z. Wu, C. Hwang, F. Wang, and Z. Q. Qiu, Creation of skyrmions in van der Waals ferromagnet Fe_3GeTe_2 on $(Co/Pd)_n$ superlattice, Sci. Adv. **6**, eabb5157 (2020).

[74] X. Jiang, Q. Liu, J. Xing, N. Liu, Y. Guo, Z. Liu, and J. Zhao, Recent progress on 2D magnets: Fundamental mechanism, structural design and modification, Appl. Phys. Rev. **8**, 031305 (2021).

[75] C. Gong and X. Zhang, Two-dimensional magnetic crystals and emergent heterostructure devices, Science **363**, eaav4450 (2019).

[76] A. S. Ahmed, J. Rowland, B. D. Esser, S. R. Dunsiger, D. W. McComb, M. Randeria, and R. K. Kawakami, Chiral bobbers and skyrmions in epitaxial FeGe/Si(111) films, Phys. Rev. Mater. **2**, 041401(R) (2018).

[77] J. Rowland, S. Banerjee, and M. Randeria, Skyrmions in chiral magnets with Rashba and Dresselhaus spin-orbit coupling, Phys. Rev. B **93**, 020404(R) (2016).

[78] M. Schott, L. Ranno, H. Béa, C. Baraduc, S. Auffret, and A. Bernand-Mantel, Electric field control of interfacial Dzyaloshinskii-Moriya interaction in $Pt/Co/AlO_x$ thin films, J. Magn. Magn. Mater. **520**, 167122 (2021), Magnetic Materials and Their Applications: In Memory of Dominique Givord.

[79] B. Dai, M. Jackson, Y. Cheng, H. He, Q. Shu, H. Huang, L. Tai, and K. Wang, Review of voltage-controlled magnetic anisotropy and magnetic insulator, J. Magn. Magn. Mater. **563**, 169924 (2022).

[80] K. Nawaoka, S. Miwa, Y. Shiota, N. Mizuochi, and Y. Suzuki, Voltage induction of interfacial Dzyaloshinskii–Moriya interaction in Au/Fe/MgO artificial multilayer, Appl. Phys. Express **8**, 063004 (2015).

[81] X. Ma, G. Yu, X. Li, T. Wang, D. Wu, K. S. Olsson, Z. Chu, K. An, J. Q. Xiao, K. L. Wang, and X. Li, Interfacial control of Dzyaloshinskii-Moriya interaction in heavy metal/ferromagnetic metal thin film heterostructures, Phys. Rev. B **94**, 180408(R) (2016).

[82] H. Yang, O. Boulle, V. Cros, A. Fert, and M. Chshiev, Controlling Dzyaloshinskii-moriya interaction via chirality dependent atomic-layer stacking, insulator capping and electric field, Sci. Rep. **8**, 12356 (2018).

[83] A. Manchon, J. Železný, I. M. Miron, T. Jungwirth, J. Sinova, A. Thiaville, K. Garello, and P. Gambardella, Current-induced spin-orbit torques in ferromagnetic and antiferromagnetic systems, Rev. Mod. Phys. **91**, 035004 (2019).

[84] P. B. Wiegmann, Superconductivity in strongly correlated electronic systems and confinement versus deconfinement phenomenon, Phys. Rev. Lett. **60**, 821 (1988).

[85] R. Shankar, Holes in a quantum antiferromagnet: A formalism and some exact results, Nucl. Phys. B **330**, 433 (1990).

[86] W.-M. Zhang, D. H. Feng, and R. Gilmore, Coherent states: Theory and some applications, Rev. Mod. Phys. **62**, 867 (1990).

[87] M. Stone, Supersymmetry and the quantum mechanics of spin, Nucl. Phys. B **314**, 557 (1989).

[88] J. Maciejko and G. A. Fiete, Fractionalized topological insulators, Nat. Phys. **11**, 385 (2015).